HHS Public Access

Author manuscript

Nat Metab. Author manuscript; available in PMC 2023 July 03.

Published in final edited form as:

Nat Metab. 2021 August ; 3(8): 1058–1070. doi:10.1038/s42255-021-00438-z.

Exercise hormone irisin is a critical regulator of cognitive function

Mohammad R. Islam[1,11], **Sophia Valaris**[1,11], **Michael F. Young**[1], **Erin B. Haley**[1], **Renhao Luo**[1], **Sabrina F. Bond**[1,2], **Sofia Mazuera**[1,2], **Robert R. Kitchen**[1], **Barbara J. Caldarone**[3], **Luis E.B. Bettio**[4], **Brian R. Christie**[4], **Angela B. Schmider**[5], **Roy J. Soberman**[5], **Antoine Besnard**[6], **Mark P. Jedrychowski**[7], **Hyeonwoo Kim**[7], **Hua Tu**[8], **Eunhee Kim**[9,10], **Se Hoon Choi**[9,10], **Rudolph E. Tanzi**[9,10], **Bruce M. Spiegelman**[7], **Christiane D. Wrann**[1,10,12,*]

[1]Cardiovascular Research Center, Massachusetts General Hospital and Harvard Medical School, Charlestown, MA 02129

[2]Program in Behavioral Neuroscience, Northeastern University, Boston, MA 02115

[3]Harvard NeuroDiscovery Center, Brigham and Women's Hospital and Harvard Medical School, Boston, MA 02115

[4]Division of Medical Sciences, University of Victoria, Victoria BC, V8P 5C2, Canada

[5]Nephrology Division, Department of Medicine, Massachusetts General Hospital and Harvard Medical School, Charlestown, MA 02129

[6]Center for Regenerative Medicine, Massachusetts General Hospital and Harvard Medical School, Boston, MA 02114

[7]Department of Cancer Biology, Dana-Farber Cancer Institute and Department of Cell Biology, Harvard Medical School, Boston, MA 02215

[8]LakePharma, Inc., San Carlos, CA 94070, USA

[9]MassGeneral Institute for Neurodegenerative Disease, Genetics and Aging Research Unit, Department of Neurology, Massachusetts General Hospital, Harvard Medical School, Charlestown, MA 02129

*Correspondence: cwrann@mgh.harvard.edu (C.D.W.).

AUTHOR CONTRIBUTIONS STATEMENT

M.R.I, S.V., M.F.Y., R.L., E.B.H., S.F.B., S.M. and C.D.W. performed and analyzed the *in vivo* experiments. S.V., E.B.H., M.R.I., and S.F.B. performed and analyzed the *in vitro* experiments. M.P.J. provided conceptual and experiment advice on the irisin plasma analysis. R.R.K. performed bioinformatical analysis. L.E.B.B. and B.R.C. conceived, performed, and analyzed the electrophysiological experiments. A.B.S. and R.J.S. performed and analyzed the dSTORM microscopy. H.T. and E.K. contributed to the data interpretation. H.K. and B.M.S designed and generated AAV8-irisin with the Penn Vector core. B.J.C., S.H.C, and R.E.T. provided scientific input. B.M.S. provided conceptual advice. C.D.W. directed the research. M.R.I, S.V., and C.D.W. cowrote the paper with assistance from all other authors.

COMPETING INTERESTS STATEMENT

The authors declare the following competing interests: B.M.S and C.D.W. hold a patent related to irisin (WO2015051007A1). B.M.S. and C.D.W. are academic co-founders and consultants for Aevum Therapeutics. C.D.W. has a financial interest in Aevum Therapeutics, a company developing drugs which harness the protective molecular mechanisms of exercise to treat neurodegenerative and neuromuscular disorders. Dr. Wrann's interests were reviewed and are managed by Massachusetts General Hospital and Mass General Brigham in accordance with their conflict of interest policies. The other authors declare no competing interests.

[10]McCance Center for Brain Health, Massachusetts General Hospital, Boston, MA 02114

[11]These authors contributed equally.

[12]Lead contact.

Abstract

Identifying secreted mediators driving the cognitive benefits of exercise holds great promise for the treatment of cognitive decline in aging or Alzheimer's disease (AD). Here, we show that irisin, the cleaved and circulating form of the exercise-induced membrane protein FNDC5, is sufficient to confer the exercise benefits on cognitive function. Genetic deletion of FNDC5/irisin (global F5KO mice) impairs cognitive function in exercise, aging, and AD. Diminished pattern separation in F5KOs can be rescued by delivering irisin directly into the dentate gyrus, suggesting that irisin is the active moiety. In F5KO mice, adult-born neurons in the dentate gyrus are morphologically, transcriptionally, and functionally abnormal. Importantly, elevation of circulating irisin levels by peripheral delivery of irisin via adeno-associated viral overexpression in the liver, results in enrichment of central irisin and is sufficient to improve both the cognitive deficit and neuropathology in AD mouse models. Irisin is a crucial regulator of cognitive benefits of exercise and potential therapeutic for treating cognitive disorders including AD.

Keywords

FNDC5; irisin; exercise; learning and memory; neurogenesis; pattern separation; hippocampus; Alzheimer's disease

INTRODUCTION

Preserving cognitive function is a major challenge in an increasingly aging population. Despite best efforts, traditional approaches to develop effective therapies have been largely unsuccessful. Interestingly, exercise, especially endurance exercise, is known to have beneficial effects on brain health and can improve cognitive function during aging[1–3]. Furthermore, higher physical activity levels are associated with reduced risk of Alzheimer's disease (AD) and lesser cognitive decline in AD [4]. These positive effects are in part due to enhanced adult hippocampal neurogenesis and synaptic plasticity in the dentate gyrus (DG) of the hippocampus as well as reduced neuroinflammation[5–7]. Identification of secreted factors that may mediate these neuroprotective effects of exercise represent very attractive drug targets.

FNDC5 (fibronectin-domain III containing 5) is a glycosylated type 1 membrane protein and has been identified as an important exercise regulated factor that induces major metabolic benefits[8]. Exercise also induces hippocampal *Fndc5* expression in mice and FNDC5 can activate hippocampal neuroprotective genes[9]. FNDC5 is proteolytically cleaved and the N-terminal portion of this is released into the circulation; the secreted form of FNDC5 has been named irisin (Fig. 1a). Irisin contains 112 amino acids, is heavily glycosylated and is 100% conserved between mouse and human. The structure of irisin and its elevation

with endurance exercise in humans has been confirmed using tandem mass spectrometry of human plasma[10]. In bone and fat, irisin mediates its effects via αV integrin receptors[11].

Although previous work has implicated the FNDC5-pathway in exercise benefits and in AD[9,12], it remains unknown whether irisin itself, the cleaved, circulating part of FNDC5, rather than the full-length membrane-bound form, is the active moiety. From a translational point of view, having the neuroprotective effects conferred in a small natural hormone versus a membrane protein is significant. Here, we show that genetic deletion of FNDC5/irisin impairs cognitive function in exercise, aging, and AD, in part by alterations of adult newborn neurons in the hippocampus. We further determine that irisin is the active moiety mediating the cognitive benefits. Most importantly, we demonstrate that peripheral application of irisin is sufficient to rescue the cognitive decline in mouse models of AD.

RESULTS AND DISCUSSION

Irisin deletion impairs cognitive function in exercise and aging

To investigate the physiological role of FNDC5/irisin in exercise, we generated *Fndc5*$^{fl/fl}$-targeted mice and crossed them with germline EIIa-cre mice to generate global *Fndc5* knock-out mice (F5KO). The flox targeting construct was designed to delete exon 3 and 4, and thereby irisin portions of the *Fndc5* gene) (Extended Data Fig. 1a). The mice were born in an approximate Mendelian ratio with no gross abnormalities and no significant difference in bodyweight (Extended Data Fig. 1b). QPCR verified loss-of-*Fndc5* mRNA expression in all tissues examined (Extended Data Fig. 1c). We used several commercial ELISA/EIAs employed in the field to quantify plasma irisin field [12], but they measured the same “irisin” concentration in the plasma of F5KO and WT mice, indicating sensitivity or specificity issues (Extended Data Fig. 1d, e). To ensure no confounding (loco-)motor deficiencies, F5KO underwent rotarod, grip strength, treadmill gait analyses, and the open field test (OPF). We observed no significant differences between genotypes in young mice (Extended Data Fig. 1f–i).

Running exercise has been shown to improve spatial learning and memory, even in young mice[5]. Further, running, not an enriched environment, is the key factor for enhancing cognitive function and adult hippocampal neurogenesis[13–15]. To assess the role of FNDC5/irisin in the exercise-induced improvements in spatial learning and memory, both WT and F5KO mice were exercised with voluntary free-wheel running and tested in the Morris water maze (MWM). Both WT and F5KO mice exercised the same amount (Extended Data Fig. 1j), but F5KO mice failed to show the exercise-induced improvements in spatial learning and memory seen in WT mice. Running shortened latency in WT mice but not F5KO mice during the MWM reversal phase (Fig. 1b). Furthermore, WT-run had better spatial memory retention in the 24hr probe trial than their sedentary control group, but F5KO-run did not (Fig. 1c). There was no significant difference between the groups in the MWM acquisition phase (Extended Data Fig. 1k, l).

Since exercise has been shown to protect against cognitive decline in aging[1,16], we next evaluated FNDC5/irisin as a crucial regulator of cognitive function in aging. Because F5KO mice showed a significantly reduced swim speed at 9-months-of-age, the novel

object recognition task (NOR) instead of the MWM was used to evaluate memory in aging (Extended Data Fig. 1m). The NOR relies on multiple brain regions, including the hippocampus. To ensure memory retention in aged WT, we used a multiday training paradigm. Young mice (8–10 weeks) showed no difference in their NOR performance; both genotypes preferred the novel object (Fig. 1d, Extended Data Fig. 1n). However, aged F5KO (21–24 months old) had more cognitive decline than aged WT, showing no preference towards the novel object (Fig. 1e, Extended Data Fig. 1o). No significant differences in bodyweight, OPF, or SAB were observed between genotypes in aged mice (Extended Data Fig. 1p–r).

Hippocampal synaptic plasticity, specifically long-term potentiation (LTP), is enhanced in the DG but not CA1 region by running, and is important for exercise's learning and memory effects[5]. Although application of high-frequency stimulation (HFS) of the medial performant pathway (MPP) produced an identical degree of post-tetanic potentiation, F5KO mice were not able to sustain LTP as well as the WT mice. At 60 min post-HFS, LTP was reduced by 37% compared to WT (Fig. 1f–i). No significant differences in fEPSP evoked for Input/Output curves and the paired pulse ratio indicate that basic synaptic transmission and presynaptic transmitter release are equivalent (Extended Data Fig. 1s, t). Taken together, these data demonstrate that genetic deletion of FNDC5/irisin impairs cognitive function in exercise and aging. In addition, the data point to a role for FNDC5/irisin in the DG. Of note, a deficit in the MWM, especially the reversal, is consistent with a defect in DG[17,18].

Pattern separation in F5KO mice can be rescued by irisin

The DG plays an important role in pattern separation[19,20]. Pattern separation, the process of minimizing overlap between similar neural inputs, is enhanced by exercise and reduced early in aging and AD, in both mice and humans[3,21–24]. Behaviorally, pattern separation/context discrimination can be evaluated by certain assays, such as the contextual fear conditioning discrimination learning paradigm (CFC-DL)[25,26], in which mice learn to distinguish two similar contexts A and B. The more similar context B is to context A, the more difficult the task. To address how FNDC5/irisin ablation affects pattern separation, we performed the CFC-DL in F5KO mice. On training days, mice were exposed to context A paired with a mild electric shock. On test days (days 2 and 6), freezing was measured as proxy for memory in both context A (without shock) and context B (Fig. 2a). To avoid presentation order becoming a confounder, half the mice in each group were presented first with context A and then with B, and the other half was presented first with context B, then A. To rule out a more anxious disposition as bias, we tested for anxiety- and depression-like behavior using the elevated plus maze and the tail suspension test, detecting no differences between genotypes (Extended Data Fig. 2a, b). While WT mice successfully discriminated between contexts as early as day 2, the F5KO only learned this task at day 6 (Fig. 2a). Interestingly, in a CFC paradigm with a more dissimilar context (context C), F5KO mice were able to distinguish between contexts comparably to the WT mice (Fig. 2b). This supports the notion that F5KOs suffer from a specific deficit in pattern separation.

To test whether irisin is sufficient to rescue the deficit in pattern separation in F5KO mice, we stereotaxically injected AAV8-irisin-FLAG directly into the DG (Fig. 2c; Extended Data

Fig. 2c). In both WT and FK5O mice, central application of irisin enhanced performance in the CFC-DL as measured by earlier context discrimination compared to the corresponding GFP-group (Fig. 2d, e). Interestingly, after stereotaxic surgery the WT-GFP mice performed worse in the CFC-DL than naïve WT mice, possibly as a result of the surgery. Of note, in all CFC-DL/CFC experiments, no significant differences were observed in baseline freezing between groups (Extended Data Fig. 2d–f). Taken together, these data suggest that irisin is the active moiety of FNDC5 that regulates pattern separation in the DG.

Adult-born neurons display aberrant activation in F5KO mice

Exercise is a well-known stimulator of neuronal activity in the DG[27,28]. To assess the function of mature granule cells and adult-born neurons in the DG, mice were exercised with free-wheel-running and injected with BrdU to label newborn neurons. Hippocampal sections were stained for c-Fos, an established marker of neuronal activity. We observed no significant difference in the number of cFos+/BrdU-/NeuN+ cells (representing mature granule cells in the DG) in dorsal hippocampal sections from F5KO compared to WT mice (Fig. 3a, b). Interestingly, we found significantly more cFos+/BrdU+/NeuN+ cells (representing adult-born neurons in the DG) in dorsal hippocampal sections from F5KO compared to WT mice (Fig. 3a, c). This was not caused by significant differences in running activity or total number BrdU+/NeuN+ cells in the DG between WT and F5KO mice (Fig. 3d–f). These results confirm that adult-born neurons in F5KO mice have an abnormal activation pattern, which could impair sparse encoding, the basis for pattern separation in the DG[29,30]. Based on this functional difference, we focused our subsequent investigations on adult-born neurons in the hippocampus.

Adult-born neurons develop abnormally in global F5KO mice

Adult-born neurons in the hippocampus play a vital role in pattern separation[21,31]. Adult hippocampal neurogenesis declines in aging and AD in mice and humans[16,32–36]. Conversely, improved adult hippocampal neurogenesis enhances learning and memory in exercise, aging, and AD[5,6,25,37]. To examine this in F5KO and WT mice, we assessed the number of newborn neurons using BrdU-labeling at baseline and did not find a significant difference between genotypes (Extended Data Fig. 3a, b). Next, we evaluated how running exercise changes newborn neuron numbers. In both WT and F5KO mice, running significantly elevated EdU+ cell numbers (Extended Data Fig. 3c, d).

Notably, exercise affects not only the number of newborn neurons but also their morphology and maturation. Running exercise increases dendritic length and complexity, raises the number of dendritic spines in the DG, and generally accelerates newborn neuron maturation[38–40]. To study newborn neuron connectivity, we stereotaxically injected a retroviral GFP-reporter (RV-CAG-GFP)[41] into the DG to sparsely label newborn neurons and examined their morphology 28 days later (Fig. 4a). Sholl analysis for dendritic complexity and total dendritic length demonstrated that dendritic arbors grew with running exercise in WT mice, as expected, but not in F5KO mice (Fig. 4b–f). Furthermore, newborn neurons in the ventral DG from sedentary F5KO mice had significantly more complex dendritic trees than those from sedentary WT mice. Of note, soma size was not affected (Extended Fig. 3e). As part of their maturation, newborn neurons undergo a phase of

dendritic outgrowth followed by a pruning [42]. Thus, the absence of FNDC5/irisin causes either overgrowth or defective pruning.

Next, dendritic spine density was analyzed in newborn neurons in the outer molecular layer of the DG. Dendritic spines represent excitatory synapses and during maturation of the newborn neurons, spines are formed and grow in size[39]. In the dorsal hippocampus, the spine density of newborn neurons was significantly less in F5KO compared to WT mice and this deficit persisted with exercise (Fig. 4g, h). In addition, dendritic spine heads in F5KO mice were smaller as measured by cumulation distribution and median size (Fig. 4i, j). In the ventral hippocampus, there was much less effect on dendritic spine density and no significant effect on spine head size (Extended Data Fig. 3f–h). A more prominent effect on dendritic spines in the dorsal than the ventral hippocampus aligns with the concept that the dorsal hippocampus is more involved in regulating cognitive function, while the ventral hippocampus governs affective behavior [43]. The reduced spines could be in response to the altered dendritic arbor to balance input activity (or vice versa). However, certain molecules, such as adhesion-GPCR BAI1, regulate dendritic outgrowth and spine density via separate mechanisms [44]. Interestingly, dendritic spine density and spine head size were not altered in mature granule cells in the DG from F5KO mice crossed with *Thy1*-GFP reporter mice, which label excitatory neurons in the forebrain, including mature granule cells in the DG (Extended Data Fig. 3i–l), supporting our hypothesis that FNDC5/irisin specifically affects newborn neuron development/maturation.

Transcriptome of adult-born neurons is altered in F5KO mice

Assessing the transcriptome of a rare cell population, such as adult-born neurons, is very challenging. Even single-cell sequencing approaches are limited for such rare cell populations[45]. Additionally, birth-dating strategies are required to target specific developmental stages in these dynamic cell populations. Here, we have developed a novel approach to ascertain the transcriptional program of newborn neurons by selectively labeling the nuclei of newborn neurons using a GFP-reporter retrovirus driven by a synapsin-promotor (RV-SYN-GTRgp) [46], followed by FACS-sorting isolated nuclei for next-gen RNA-sequencing (RNA-seq). This approach yielded 200–500 immature neuron nuclei per mouse (Fig. 5a; Extended Data Fig. 4a, b).

To confirm that our approach preferentially enriched for neuronal nuclei, we performed gene ontology analysis using DAVID[47,48] on the top 1500 expressed genes. “UP_TISSUE Brain” was the top hit (p=2.8E-84). Principal component analyses and hierarchical clustering revealed a largely abnormal transcriptional profile in newborn neurons from F5KO mice, regardless of exercise intervention (Fig. 5b). It is possible that the larger variability of nuclear RNA-seq, compared to cellular RNA-seq, left these studies underpowered to detect an exercise effect with this sample size. A total of 459 genes were differentially expressed between F5KO and WT newborn neurons ($\log_2FC > \left| 1.5 \right|$, p-value < 0.05) (Fig. 5c). Gene set enrichment analysis (GSEA) [49,50] identified important disease pathways dysregulated by loss-of-FNDC5/irisin in adult-born neurons, including “Alzheimer’s disease” as well as pathways consistent with disrupted neuronal development, e.g. “Neurotrophin signaling pathway” or “Dendrite development” (Fig. 5d). Of note, we have

performed bulk RNA-seq of microdissected DG from F5KO and WT mice. Although mature neurons contribute to ~50% of this tissue, only two genes, in addition to *Fndc5*, were differentially expressed between WT and F5KO ($\log_2$FC > | 0.5 |, p-value < 0.05) (Extended Data Fig. 4c). Taken together, these data demonstrate that lack of FNDC5/irisin alters adult-born neurons morphologically, transcriptionally, and functionally.

Peripheral irisin improves cognitive function in AD models

Hippocampal *Fndc5* gene expression is significantly reduced at six months of age in the well-established transgenic AD mouse model APP/PS1 (APPswe,PSEN1dE9)[51,52] compared to WT littermates (Fig. 6a). APP/PS1 mice develop amyloid plaques, gliosis, and cognitive deficits starting at 6-months-of-age. Analysis of RNA-seq data from the MSSM study (Mount Sinai School of Medicine, and Mayo), comprising 2,114 samples from 1,234 human subjects, showed significantly lower FNDC5 expression in the parahippocampal gyrus in patients with AD compared to controls, but not in other brain regions (Fig. 6b) [53]. Next, we crossed our F5KO mice with the APP/PS1 mice to evaluate how loss of FNDC5/irisin affects cognitive function in experimental AD. Notably, APP/PS1-F5KO performed worse than APP/PS1-WT in the CFC, failing to freeze significantly less in the alternate context compared to the training context (Fig. 6c), indicating a deficit in context discrimination. Interestingly, in the cortex, APP/PS1-F5KO showed significantly higher levels of soluble Aβ−40, which contributes to plaque formation and more dysfunctional vascular integrity [54,55], compared to APP/PS1-WT However, the hippocampus did not present such differences (Extended Data Fig. 5a, b). No significant differences between genotypes were observed in body weight, OPF and SAB, or baseline freezing in the CFC (Extended Data Fig. 5c–g).

To evaluate the therapeutic potential of peripherally delivered irisin, 8-month-old male APP/PS1 mice received AAV8-irisin-FLAG or AAV8-GFP via tail vein injections to overexpress irisin in the liver and increase circulating irisin to pharmacological levels (Fig. 6d, e; Extended Data Fig. 6a). Importantly, this resulted not in overexpression in the hippocampus (Extended Data Fig. 6b and 7b). At 10-months-of-age, irisin-treated mice performed significantly better in spatial learning and memory tasks, such as the Barnes maze or the MWM (Fig. 6f, g; Extended Data Fig. 6g–j). To avoid genotype bias and confirm the generalization of irisin's effects, we also used transgenic AD mouse model, namely 5×FAD mice [56], with AAV8-irisin in the same manner as the APP/PS1 mice. 5xFAD mice develop neurodegeneration in addition to amyloid plaques, gliosis, and cognitive deficits. In the 5xFAD mice, peripheral elevation of irisin levels resulted also in an improvement in spatial learning and memory in the MWM (Fig. 6h, i; Extended Data Fig. 7g–j). In line with our data from the global F5KO mice, irisin treatment of APP/PS1 mice improved context discrimination/pattern separation in the CFC-DL with similar contexts but did not change performance in a CFC assay with distinct context (Extended Data Fig. 6k,l and 7k, l). Similarly, we did not observe a difference with irisin treatment in the SAB (Extended Data Fig. 6f, 7f). Bodyweight and OPF performance were unaffected, indicating no obvious toxicity by forced irisin expression in the APP/PS1 or 5xFAD mice (Extended Data Fig. 6c–e, 7c–e).

Peripheral irisin reduces glia activation in AD models

Astrocyte and microglia reactivation has been reported to be involved in aging-related neurodegeneration[57,58]. Indeed, in the hippocampus of irisin-treated APP/PS1 mice, GFAP+ astrocytes and Iba1+ microglia were significantly smaller compared to GFP-treated mice (Fig. 7a, b), pointing towards reduced glial activation. Furthermore, GSEA of RNA-seq data from the hippocampus identified several pathways associated with neuroinflammation (Fig. 7c). Of note, several of these pathways identified overlapped with the pathways identified in the newborn neurons from the F5KO mice. Lastly, overrepresentation analysis revealed that astrocyte- and microglia-specific genes were significantly more downregulated in irisin-treated AD mice compared to controls than genes of all other cell types (Fig. 7d). Notably, no differences were detected in the number of BrdU+ cells and hippocampal or cortical Aβ-plaque burden (Extended Data Fig. 8c–h). We have also measured the synaptic plasticity gene described by Lourenco et al. as target genes of FNDC5 but did not observe any significant changes (Extended Data Fig. 8a).

We have recently identified αVβ5 integrins as a receptor for irisin in bone and fat cells[11] and, interestingly, the “Focal adhesion” pathway was regulated in both our RNA-seq analyses (Fig. 5c and 7c). Two-color dSTORM (direct stochastic optical reconstruction microscopy with single molecule resolution) demonstrated cell-surface binding of recombinant irisin-FLAG in neuronally-differentiated primary adult hippocampal neural stem cells cultures, which express both, αVβ3 and αVβ5 integrins (Extended Data Fig. 9a). Clus-DoC analysis on the localization maps with nano-meter scale resolution revealed that only 0.4 % [0.1, 0.5] of irisin molecules were co-localized with αVβ3 integrins whereas significantly more irisin molecules, namely 16% [5, 23], were co-localized with αVβ5 integrins (Fig. 7e, f). Single-cell RNA-seq data from the murine DG[59] showed that *Itgav* is expressed ubiquitously in neuronal and non-neuronal cells, whereas *Itgb5* is mainly expressed on astrocytes and microglia (Extended Data Fig. 9b, c). Confocal microscopy confirmed that the αVβ5 integrin receptor complexes are mainly located on astrocytes, not neurons (Fig. 7g). Of note, these cultures do not contain microglia (Extended Data Fig. 9d). Taken together, these results demonstrate that peripheral delivery of irisin is sufficient to rescue cognitive decline in two AD mouse models. Furthermore, the data indicate that the irisin effect could be mediated by irisin-regulated glia activation through αVβ5 integrin receptor complexes.

Peripherally delivered irisin crosses blood brain barrier

It is crucial to know whether the peripherally expressed irisin crosses the blood brain barrier (BBB) and has direct central effect in the brain or whether peripheral irisin induces other molecules which cross the BBB and elicit these central effects. To directly test if irisin crosses the BBB, WT mice were injected i.v. with AAV8-irisin or AAV8-GFP. Three weeks later, blood was collected. Then mice were perfused with 50 ml of PBS to remove all remaining blood, and various tissues were collected. We first confirmed that the viral expression of irisin mRNA was observed only within the liver but not within other peripheral organs. Most importantly, we did not detect any increased irisin mRNA expression within the brain, including the hippocampus (Fig. 8a, Extended Data Fig. 6b and 7b). Elevated irisin protein levels were observed in plasma and liver (Fig. 8b, c). Notably, we also detected

significantly elevated irisin protein levels within the brain but not in the quadriceps (Fig. 8c). Since we did not observe increased irisin gene expression in the brain, we conclude that these increased irisin protein levels are the result of irisin crossing the BBB. Of note, this liver-derived circulating irisin-FLAG had the expected size of ~12kDa and is glycosylated as native irisin (Extended Data Fig. 10a).

To assess irisin's effect on peripheral tissues, we performed qPCR on several peripheral organs (liver, quadriceps, inguinal white adipose tissue, interscapular brown adipose tissue) from AAV8-irisin and AAV8-GFP injected WT mice. However, we did not detect significant gene expression changes in these tissues with irisin treatment (Extended Data Fig. 10b–e). Taken together, these data strongly support our hypothesis that peripherally delivered irisin directly affects the brain.

Discussion

The identification of secreted mediators driving the cognitive benefits of exercise holds great promise for the development of treatments for the cognitive decline in neurodegeneration, such as Alzheimer's disease (AD). This promise would be greatly enhanced if these secreted factors could be administered peripherally. Here, we evaluate whether irisin, the secreted part of the exercise hormone FNDC5, confers these beneficial effects on cognitive function. We demonstrate that genetic deletion of FNDC5/irisin impairs cognitive function in exercise, aging, and AD. Furthermore, we show that the cleaved, circulating part of the hormone, called irisin is the active moiety in that it can restore cognitive function. Most importantly, we show that peripheral application of irisin, which lead to elevated central levels of irisin, is sufficient to rescue the cognitive decline in two distinct mouse models of AD – even after the development of significant pathology.

We demonstrate unequivocally that irisin itself confers the cognitive benefits by employing an AAV8 vector that only forces expression of irisin but not the parent protein FNDC5. In a previous study, Lourenco *et al.* used peripheral delivery of full-length FNDC5-adenovirus to improve cognitive function in a transgenic AD mouse model; whether these effects were through irisin or the full length FNDC5 protein thus could not be determined[12]. Importantly, we also demonstrate here that peripherally delivered irisin crosses the blood brain barrier.

Astrocytes and microglia act as important contributors to cognitive decline in aging and AD-related degeneration by increasing inflammation but also by impacting neurons directly, e.g. pruning of synapses[57,58,60]. Our data on reduced glia activation with irisin treatment in AD mouse models suggest that irisin may exert its effects through astrocytes and/or microglia. Finally, our two-color dSTORM data points towards the αVβ5 integrins as key binding partners on these cell surfaces; these integrin subunits had previously been described as the functioning receptor for irisin's action on bone and fat cells[11]. However, more mechanistic studies are required to determine this.

Adult hippocampal neurogenesis has been shown to regulate cognitive function, mainly pattern separation, in exercise, aging, and AD[5,6,16]. Adult-born neurons from F5KO mice lack the exercise-induced increase in dendritic complexity, have lesser and smaller spines,

and an altered transcriptome and neuronal activation, which is consistent with a defect in maturation[38–40,42]. This abnormal adult hippocampal neurogenesis is accompanied by impaired pattern separation, which can be rescued by irisin delivery into the DG, strongly suggesting that dysregulated adult-born neurons are, at least in part, responsible for the defect in cognitive function caused by genetic ablation of FNDC5/irisin. Interestingly, it has also been shown that changing adult hippocampal neurogenesis can rewire existing circuits in the hippocampus[37].

While our data shows that peripheral irisin application is sufficient to regulate cognitive function in AD, this does not answer whether muscle- or hippocampus-derived irisin is responsible for the cognitive benefits with exercise. To dissect the contribution of different tissues, tissue-specific KO mouse model will be needed in the future. Since FNDC5/irisin was deleted embryonically, it is possible there are development defects in the F5KO mice. However, our data strongly point to the use of irisin at pharmacological doses in treating cognitive decline at pharmacological levels. Of note, our AD transgenic models are based on mutations in genes causal for Familial Alzheimer's disease (FAD). However, since irisin does not specifically target the formation or removal of amyloid plaques, but rather targets neuroinflammation directly, we are optimistic that irisin's beneficial effects in neurodegeneration are generalizable beyond FAD. In addition, data shows that the irisin improved cognitive function, even in wild-type mice. The fact that irisin treatment was effective in AD mouse models even after the development of significant pathology is promising for translation into humans where therapy would typically start after patients are already symptomatic.

METHODS

Animal procedures and ethics statement.

All animal procedures were approved by the Institutional Animal Care and Use Committee of the Massachusetts General Hospital (MGH) and the Harvard Center for Comparative Medicine. C57BL/6J (000664, JAX) were used as wildtype mice We developed *Fndc5*$^{fl/fl}$-targeted (Exon 2 and 3) mice with the Texas A&M Institute for Genomic Medicine using homologous recombination. Global FNDC5 KO mice (F5KO) were generated by crossing *Fndc5*$^{fl/fl}$ with B6.FVB-Tg(EIIa-cre)C5379Lmgd/J mice (003724, JAX). APP/PS1 mice (34832, JAX) were crossed with a heterozygous F5KO to generate the APP/PS1-F5KO strain. All strains were on a C57BL6 background. 5xFAD mice were maintained on a mixed background at MGH (6SJL-Tg(APPSwFlLon,PSEN1*M146L*L286V)6799Vas/Mmjax). Thy1-GFP+/F5KO were generated by crossing the F5KO mice with the Thy1-GFP line M (007788, JAX). Mice were maintained in an SPF environment at MGH with 12-h light/12-h dark cycles (seven am-seven pm), at 20–22 ^{0}C temperature, and 30–70% humidity. Mice had free access to water and standard chow (Prolab® IsoPro® RMH 3000, Irradiated). Mice were group-housed, except for running experiments. For running experiments, mice were housed individually either with or without a running wheel.

Experiments were performed with sex- and age-matched littermates of the indicated genotypes. Six-week-old male F5KO mice were used for morphological experiments with RV-GFP, RNA-sequencing of GFP-labeled nuclei from newborn neurons, and

AAV8 injections into the DG. Seven-week-old male wildtype mice were used for BBB experiments. Eleven- to fourteen-week-old male wildtype mice were used for primary adult hippocampal stem cell culture. Six to eight-week-old male F5KO were used for running experiments with behavioral and tissue analysis. Eight to thirteen-week-old male and female F5KO mice were used for behavioral experiments and tissue analysis. Eight-week-old male F5KO mice were used for electrophysiological experiments. 21–23-month-old female mice were used for the aging cohort. Six-month-old male APP/PS1-F5KO mice were used for behavioral and tissue analysis. Seven-month-old male APP/PS1 and five months old male 5xFAD mice were used for behavioral and tissue analysis.

Primary Adult Hippocampal Stem Cell Cultures

Primary neural stem/progenitor cells (NPCs) were isolated from the DG and differentiated into neurons as previously described [61,62]. Neurospheres were disassociated with trypsin and plated in 6-well plates (3516, Corning Costar) coated with poly-L-ornithine (P-3655, Sigma.) and laminin (354232, BD Biosciences) at the density of 1×10^5 cells/well for all experiments.

Production of Adeno-associated Virus (AAV)

Mouse ORF 1–140 (containing the N-terminal signal peptide and irisin) plus a five amino acid linker plus C-terminal flag-tag was cloned into the pENN.AAV.CB7.CI.pm20d1flag.WPRE.rBG vector (Addgene plasmid # 132682) to replace pm20d1flag (pENN.AAV.CB7.CI.PM20D1-flag.WPRE.rBG was a gift from Jonathan Long (# 132682). The final plasmid was sequenced to confirm the correct insertion of Irisin ORF. AAV (serotype 8) was packaged at the UPenn Vector Core with a titer of 3.012E13 G.C./ml, and the MGH Vector Core Facility, with 1.66E13 G.C./ml respectively. AAV8-GFP (pENN.AAV.CB7.CI.eGFP.WPRE.rBG) was used as control, obtained from Addgene (#105542), and packaged at the UPenn Vector Core with titer 2.10E13 G.C./ml.

Stereotaxic Surgery

Mice were injected using stereotax surgery to deliver one μl of RV-CAG-GFP/RV-SYN-GTRgp or AAV8-GFP or AAV8-irisin-FLAG (titer 1E13/ml) to the dentate gyrus as described previously [63]. For details please refer to the supplementary method section.

Tail vein injections

Mice were injected under isoflurane anesthesia into the tail vein with AAV8-GFP or AAV8-Irisin-FLAG (1E10 G.C./mouse) diluted in PBS to a final volume of 100 μl.

Running Exercise Paradigm

Mice were weighed and were placed individually in cages with stainless steel running wheels (Starr Life Sciences) (running) or without (sedentary controls). Running activity was tracked using a revolution counter that collected data every hour (VitalView Animal Activity v1.4, Starr Life Science). For running-induced c-Fos activation, the recording was set to 30 mins intervals during the last 90 mins of running.

Behavioral Assays

For behavioral evaluation, Open field test (OPF)[64], Rotarod[64], Grip strength[65], Tail suspension test (TST)[66], Elevated plus maze (EPM)[67], Gait analysis[64], Morris water maze (MWM)[68,69], Contextual fear conditioning (CFC)[67], Contextual fear conditioning-discrimination learning (CFC-DL)[25,26], Novel object recognition (NOR)[70], Spontaneous alternation behavior (SAB)[71], Barnes maze[72] were performed as described previously with modification. For a detailed description, please refer to the supplementary method section.

Antibody list

All primary and secondary antibodies with source, dilutions, and validations are listed in supplementary data Tables 1 and 2, respectively.

BrdU and EdU labeling

Mice were injected daily intraperitoneally (i.p.) with BrdU (50 mg/kg, (Sigma, dissolved in 0.9% saline,) or EdU (50mg/kg, Abcam, dissolved in PBS). Solutions were filtered at 0.22 μm. EdU was dissolved in 1X PBS and filtered at 0.22 μm. At the end of the experiment, the mice were anesthetized with isoflurane and perfused transcardially. For a detailed description on time-course of the injection in each experiment, please refer to the supplementary method section.

Immunohistochemistry and microscopy

Immunofluorescence (IF) and immunohistochemistry (IHC) staining were done following the methods described previously [6]. Briefly, PFA-fixed and cryoprotected brains were cryosectioned. Staining was performed on 35 μm coronal free-floating sections (one-in-six series) from embedded tissue. For IF antibodies for GFP, 3D6, FLAG, GFAP, IBA1, MAP2, aVb3 integrins, and aVb5 integrin were used. For anti-BrdU staining, sections were pretreated for antigen retrieval. BrdU IHC was completed using the ABC peroxidase complex (ABC Kit, Vector Laboratories) with DAB (Sigma). To label sections for EdU-positive cells, we used the Click-iT EdU Cell Proliferation Kit (Invitrogen) as described previously [22]. For a detailed description, please refer to the supplementary method section.

BrdU and EdU quantification

Counting of positive cells followed the principle for design-based stereology for AHN as outlined in [73] using a light microscope (TE360 Eclipse, Nikon), a fluorescence microscope (Axio Imager, A2, Zeiss), or a confocal microscope (LSM 780, Zeiss).

c-Fos detection and quantification

The dorsal DG was imaged in Z-stack mode using a confocal microscope (LSM 780, Zeiss) in 20X for three sections from matching bregmas. Images for each Z-stack were taken 2 μm apart for a total Z-stack of 14–16 μm. Maximum projected images were created in ImageJ (v2.0.0-rc-69/1.53c), and used to quantify the BrdU+/c-Fos+/NeuN+ and BrdU-/c-Fos+/NeuN+ cells in the granular cell layer (GCL) and subgranular zone (SGZ).

Glial cell and amyloid plaque quantification

Quantitative analysis of glial cells and amyloid plaque in hippocampal sections and/or cortex was performed using a previously described protocol [74]. For a detailed description, please refer to the supplementary method section.

Morphological analysis

Dendritic complexity and spine morphology were analyzed following the methods described previously[37]. For a detailed description, please refer to the supplementary method section.

Electrophysiological Analysis

Electrophysiological analysis was performed according to the protocol described previously [75,76] with slight modifications. Detailed method can be found in the supplementary method section.

ELISA/EIA

Blood was collected via the posterior vena cava in heparin-coated tubes (365985, BD Microtainer) and then centrifuged. The plasma fraction was collected and stored at −80°C until analysis. Irisin EIA and ELISA (EK-67-16 and EK-067-29, Phoenix Pharmaceuticals) were performed according to the manufacturer's instructions. For Meso Scale Discovery (MSD) ELISAs, hippocampal and cortical tissues were homogenized in RIPA buffer (Sigma) and centrifuged at 45,000 g for 30 min at 4°C. Supernatants were used to measure the soluble fraction of Aβ peptides 40 and 42 using the 96-well V-PLEX Plus Aβ peptide panel 1 (6E10) kit as outlined in the manufacturer's protocol and was read on a Meso QuickPlex SQ 120.

For the irisin-FLAG ELISA, 96 well plates were coated with an anti-irisin capture antibody in PBS overnight at 4°C. The next day, plates were washed four times with 0.1% PBST and blocked with 1% BSA for one hr RT. After four washes with 0.1%, PBST, standards (0–200 ng/ml) and plasma samples were added to the plate and incubated for two hrs at RT. Plates were incubated with an Anti-FLAG detection antibody for two hrs in RT after washing 4X with 0.1% PBST. Next, the samples were incubated in HRP-linked secondary antibody for 30 min following 4X PBST wash. 3,3',5,5'-Tetramethylbenzidine (TMB) chromogen (ab171522, Abcam) was used as detection systems, and finally, the absorbance was measured at 450nm after adding stop solution (ab171529, Abcam) using a plate reader (FLUOstar Omega, BMG Labtech). Irisin-FLAG concentration was quantified from the standard curve of recombinant irisin-FLAG (AG-40B-0136-C010, Adipogen)

Western blot for irisin-FLAG in plasma

Plasma samples (10μl) were depleted of albumin and IgG with Proteome purify 2 mouse serum protein Immunodepletion Resin (MIDR00204, R&D Systems). Samples (100 ug of protein) were subsequently precipitated with trichloroacetic acid (TCA, 0.2% deoxycholate sodium in 100% TCA) and incubated overnight at 4°C. After multiple methanol washes, briefly dried protein pellets were resuspended in 18μl H_2O and deglycosylated with the Protein Deglycosylation Mix (P6044S, New England Biolabs) as per the manufacturer's

denaturing protocol overnight. Deglycosylated plasma samples, after adding SDS-Sample buffer with 10 mm DTT (Sigma) were separated on precast 4–12% NuPAGE Bis-Tris gradient gels (NP0335BOX, Thermofisher Scientific) with MES buffer (NP0002, Novex). Gels were transferred to a PVDF membrane (88520, Thermo Scientific). Membranes were blocked with 5% bovine serum albumin (Sigma), probed overnight at 4°C with anti-FLAG, and incubated for two hrs at room temperature with horseradish peroxidase-conjugated secondary antibody, and chemiluminescence was detected with Supersignal West Pico Plus chemiluminescence substrate (34577, Thermo Scientific).

RNA Preparation and Expression Analysis

Total RNA was isolated from tissues or culture cells using TRIzol (Invitrogen) and the QIAGEN RNeasy mini or QIAGEN RNeasy micro kits, respectively, according to the manufacturer's instructions. For qPCR analysis, the first-strand cDNA was generated using a High-Capacity cDNA Reverse Transcription Kit with RNase Inhibitor (4374967, Thermo Fisher Scientific). qPCR was performed using Power SYBR Green PCR Master Mix (4367660, Thermo Fisher Scientific) in a QuantStudio5 Real-Time PCR system (Applied Biosystems). mRNA quantities were normalized to Rps18 after determination by the comparative Ct method [77]. Primer sequences are shown in supplementary Data Table 3.

Isolation, sorting, and RNA-sequencing newborn neuron nuclei

Here, we have developed a novel approach to ascertain the transcriptional program of newborn neurons by selectively labeling the nuclei of newborn neurons using a GFP-reporter retrovirus driven by a synapsin-promotor (RV-SYN-GTRgp) followed by FACS-sorting isolated nuclei for next-gen RNA-sequencing. A detailed method can be found in the supplementary method section.

RNA-sequencing of tissues other than newborn neurons

Bulk RNA-sequencing was performed using the hippocampal tissues from APP/PS1 mice injected with AAV8-irisin-FLAG or AAV8-GFP. RNA extraction, library preparations, and sequencing reactions were conducted at GENEWIZ, LLC. (South Plainfield, NJ, USA). Bulk RNA-sequencing was performed on microdissected DGs from F5KO and WT mice. Library preparations, and sequencing reactions were conducted by the Dana-Farber Cancer Institute Molecular Biology Core Facilities. For a detailed description, please refer to the supplementary method section.

Differential Expression analysis

Per-sample transcript-level were quantified and gene-level counts are filtered. DESeq2 (v1.10.1, R/Bioconductor package) was used for normalization and to determine differentially expressed genes. For the detailed method, please refer to the supplementary method section.

Pathway / Gene-set Enrichment Analysis

Differentially expressed genes were interrogated for gene-set / ontology/pathway enrichments using the R packages DOSE (v3.9.4, Bioconductor), clusterProfiler (v3.12.0,

Bioconductor), and Pathview (v3.9, Bioconductor). Enrichments are computed for Gene Ontology (GO) terms and KEGG pathways against the background set of detected genes and filtered to retain significant enrichments using BH-corrected p-Values < 0.05.

Overrepresentation analysis

Genes were categorized as either 'astrocyte'- or 'microglia'- markers based on their classification in the Dropviz single-cell sequencing database in the mouse hippocampus (http://dropviz.org)[45]. All remaining genes (that are not markers of these cell types) were classified as 'none'. Irisin/GFP expression ratios for all genes were plotted according to these cell-type labels and two-tailed t-tests were used to compare the distributions of astrocyte and microglia Irisin/GFP ratios to the 'none' control, respectively.

RNA-sequencing data analysis from the MSSM study

FNDC5 differential expression data for human AD vs Control subjects were obtained from the MSSM RNA-sequencing study (Mount Sinai School of Medicine, and Mayo; MSSM_FP_STG_PHG_IFG_DiffExpression.tsv) [53]. Log2-fold change and FDR adjusted p-values were plotted for each of the four brain regions profiled in this study.

Direct stochastic optical reconstruction microscopy (dSTORM)

Primary neural stem/progenitor cells (NPCs) were seeded on eight-well chamber slides (Ibidi) coated with poly-L-ornithine (P-3655, Sigma) and laminin (354232, BD Biosciences) and differentiated as described above. On day seven of differentiation, the medium was changed to FreeStyle293 Expression medium (Gibco). After a four-hour incubation followed by ten minutes on ice, the cells were incubated with 10nM recombinant irisin-FLAG (Adipogen) for 20 minutes. After two washes with ice-cold PBS, cross-linking was performed with 1.5mM DTSSP for 30 minutes at 4 degrees. Then Tris-pH 7.5 was added to a final concentration of 20mM to quench cross-linking. Two-color dSTORM experiments were performed using anti-integrin aVb3 anti-integrin aVb5, and anti-FLAG-tag following the method described previously [78].

Quantification of blood-brain barrier permeability of irisin

Mice were injected with AAV8-GFP or AAV8-irisin-FLAG in the tail vein (10e10/mouse). Twenty-one days later, under isoflurane anesthesia, plasma was collected from the vena cava caudalis, and mice were perfused with 50 ml cold PBS. Tissues were collected and snap-frozen in liquid nitrogen. "Irisin" gene expression using qPCR was performed as described above. Levels of irisin-FLAG protein in plasma and tissue lysates were measured using the irisin-FLAG sandwich ELISA described above.

Data Availability Statement

RNA-seq datasets are available at the Gene Expression Omnibus (GEO) repository under accession super serial number GSE174212, which contains GSE174210, GSE174211, and GSE179078 datasets. Markers for astrocytes and microglia are available from http://dropviz.org. Data from the MSSM study is available from www.synapse.org. The single-cell

data is available from http://linnarssonlab.org/dentate. Any other relevant data are supplied in the Source files.

Code Availability Statement

The code for the RNA-sequencing data analysis from the MSSM study is available in the Supplementary Information.

Statistical analyses.

Statistical analysis was performed using GraphPad Prism 9.1 (216). Significance was assigned to differences with a p-value less than 0.05 unless stated otherwise. Data are expressed as mean ± s.e.m. unless stated otherwise. Two-tailed Student's t-tests were used to compare two groups with a Welch's correction if variances were significantly different between groups. For comparisons among multiple groups, one-way, two-way, or repeated-measures ANOVA followed by the indicated *post-hoc* test was used. Multiple t-tests were performed with Bonferroni-Dunn method correction for adjusted p-values. To be able to perform repeated-measures ANOVA missing values were substituted using a mean substitution. Spine head diameter distribution was assessed using the Kolmogorov-Smirnov test when comparing two groups or the Kruskal-Wallis test when comparing more than two groups and significance was assigned to differences with a p-value less than 0.001. For behavioral analysis, experiments were either performed as one cohort (Fig. 1d–e, ED Fig. 1n–r, Fig. 2a–b, ED Fig. 2c–d, Fig. 6f, ED Fig. 6g, Fig. 6g, ED Fig. 6h–m, Fig. 6i, ED Fig. 7g–j) or in separate smaller cohorts (Fig. 1b, c, ED Fig. 1k, l, Fig. 2d, ED Fig. 2f, Fig. 6c, ED Fig.5d–g, ED Fig. 6c–f, Fig. 7d–f, k–l) and the statistical analysis was performed on the complete data set. Samples size was based on previously published studies using similar methodologies. Outliers were identified using the Grubbs' test with a significance level of $p<0.05$ (two-sided). For behavioral tests, exclusion criteria were pre-established following published guidance [71,79,80]. In the SAB, mice with less than 8 arm entries during the 5-min trial were excluded from the analysis as significantly lower exploratory activity biases the analysis. In the CFC, mice that did not freeze after receiving the shocks on day 1 were excluded from that analysis as we cannot use freezing as a proxy for learning or memory. In the NOR, mice that spend less than 10 sec interacting with the objects were excluded since low exploratory activity biases the analysis. For all experiments, all stated replicates are biological replicates. Operators were blinded to the true experimental groups during data collection and image analysis by de-identifying all samples with generic unique IDs.

Extended Data

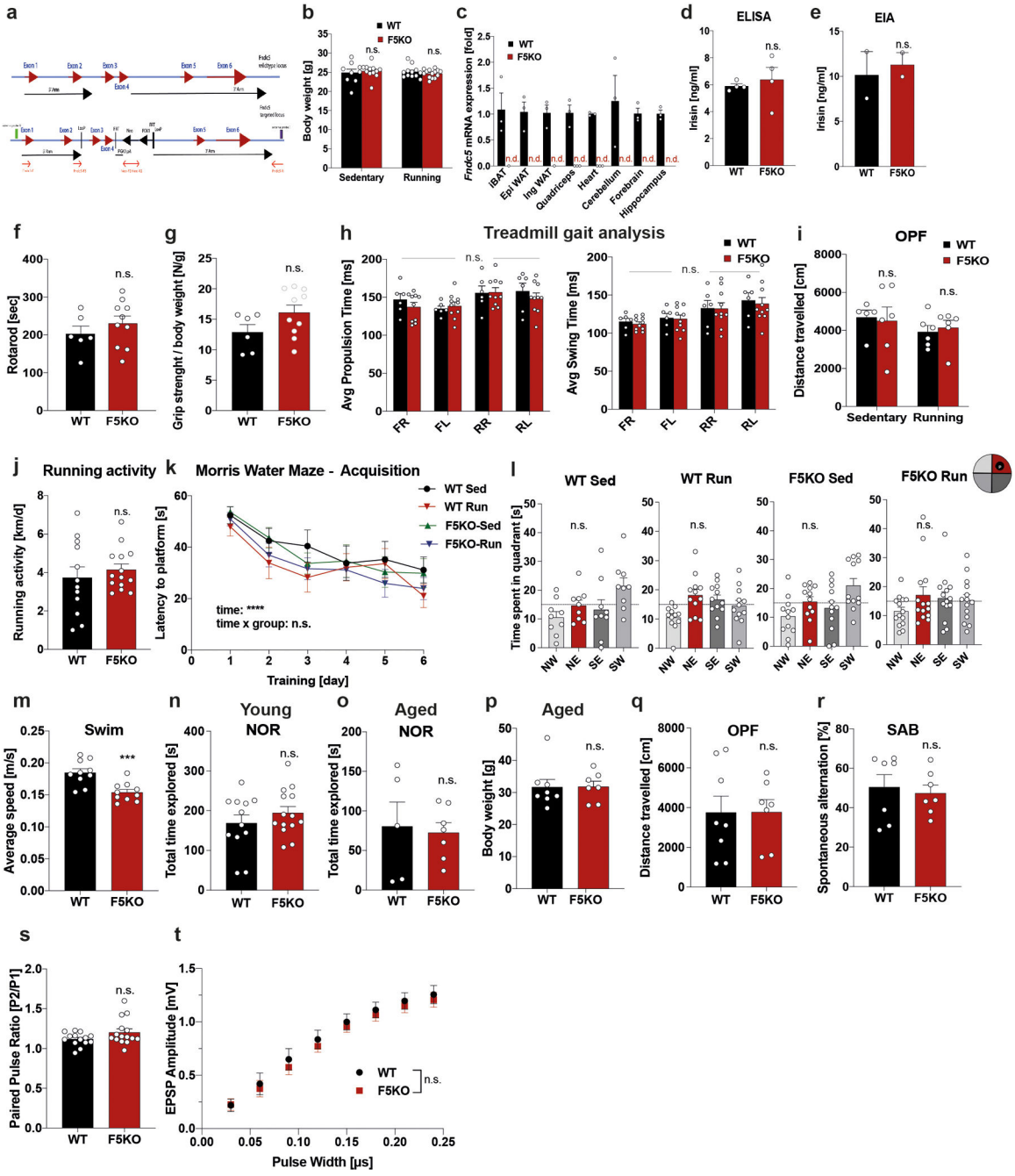

Extended Data Fig. 1: Irisin deletion impairs cognitive function in exercise and aging.

a, Schematic of flox targeting-construct for the *Fndc5* locus. **b,** Bodyweights (WT-sed n = 9; WT-run n = 12; F5KO-sed n = 12; F5KO-run, n = 14). **c,** qPCR of *Fndc5* mRNA expression (n.d.: no detection) (n = 3 per group). **d and e,** Plasma irisin with commercial ELISA (n = 4 per group) (**d**) or EIA (n = 2 per group) (**e**). **f,** Rotarod, **g,** Grip strength, **h**, Gait scan analysis: average propulsion (left) and swing time (right). FR = front right limb, FL = front left, RR = rear right, RL = rear left (WT n = 6, F5KO n = 10), **i**, Open field test (OPF)

(WT-sed n = 5; WT-run n = 6; F5KO-sed n = 6; F5KO-run n = 6), and **j,** Running activity and **k and l,** Morris-water-maze (MWM): latency to reach target platform **(k)** and 24h probe trial in acquisition **(l)**. NE (red bar) was the target quadrant (WT-sed n = 9; WT-run, n = 12; F5KO-sed n = 12; F5KO-run, n = 14). **m,** Swim speed, 9-months-old mice (WT, n = 10, F5KO, n = 10). **n** and **o,** Novel object recognition (NOR) task in young **(n)** (WT n = 12, F5KO, n =14) and aged mice **(o)** (WT n = 5, F5KO, n =7). **p and q,** Bodyweights **(p)** and Open field test (OPF) **(q)** for aged mice (WT n = 8, F5KO, n = 7). **r,** Spontaneous alternation behavior (SAB) in aged mice (WT, n = 7, F5KO, n = 7). **s and t,** Electrophysiology in DG using acute slices, paired pulse ratio (**s**) and EPSP input-output curve (**t**) (WT n = 14, F5KO n = 15 slices, 7 animals per group,). RM-Two-way ANOVA (**k, t**), Two-way ANOVA (**b**, **h**, **i**), One-way ANOVA. Significance was assigned only if time spent in the target quadrant was significantly different from all other quadrants (**l**), Two-tailed t-test (**d-g**, **j, m-s**). ***p<0.001, ****p<0.0001 n.s.= not significant. Data represented as mean ± SEM of biologically independent samples. See source data for exact p-values.

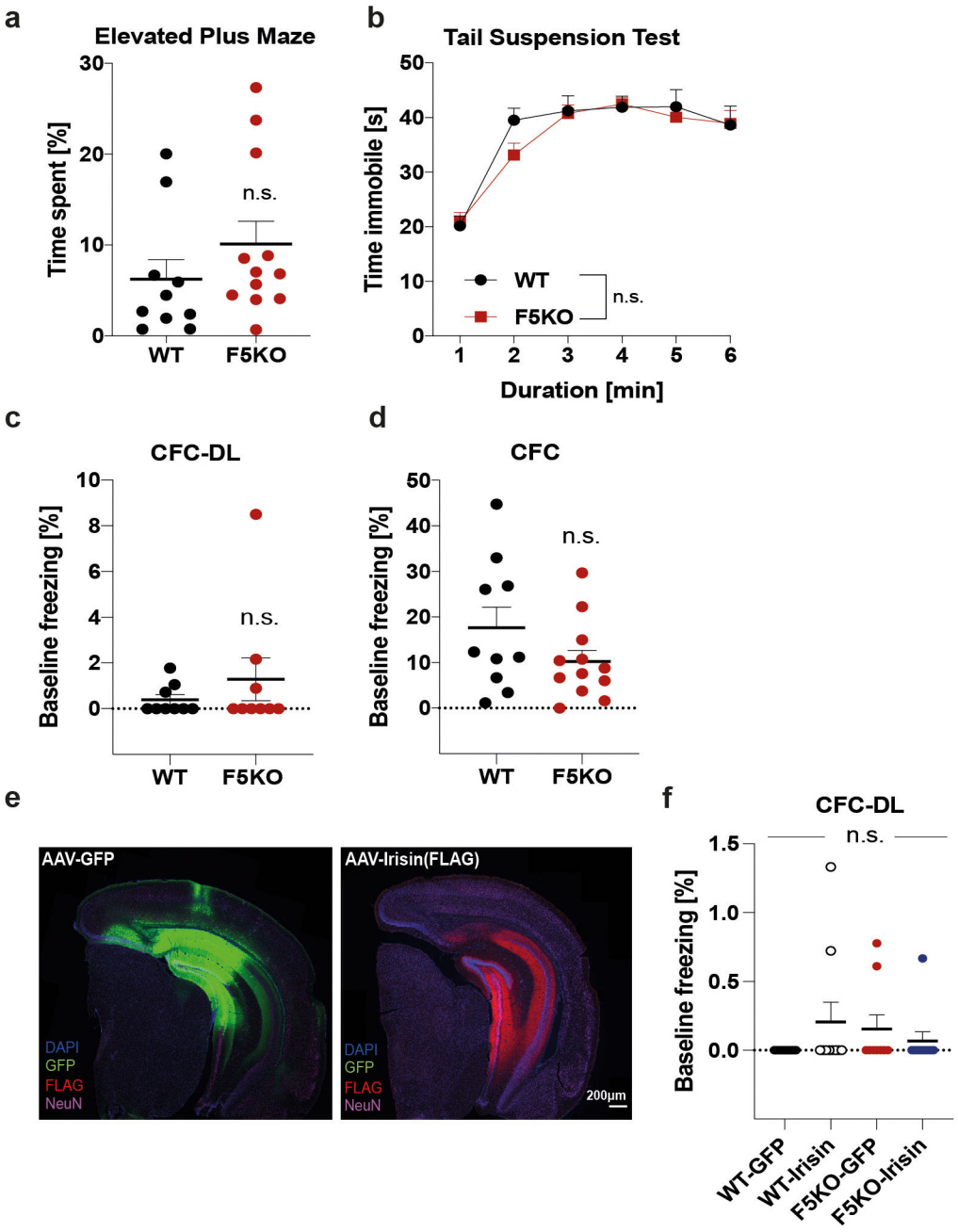

Extended Data Fig. 2: Pattern separation is impaired in F5KO mice and can be rescued by delivering irisin directly into the dentate gyrus.

a, Elevated plus maze. **b,** Tail suspension test. **c and d**, Baseline freezing in CFC-DL (**c**) and in CFC (**d**) of WT and F5KO mice. **e and f,** WT and F5KO stereotaxically injected with AAV8-GFP or AAV8-irisin-FLAG into the DG. Representative immunofluorescence images, GFP (green), irisin-FLAG (red), NeuN (magenta) in the hippocampus. Scale bar 200 µm (**e**) and baseline freezing in the CFC-DL (**f**) (WT n = 10, F5KO n = 12 (**a, b, d**); n = 9 per group (**c**); WT-GFP n = 10, WT-irisin n = 10, F5KO-GFP n = 9, F5KO-irisin n= 10 (**f**)). RM-Two-way ANOVA (**b**), One-Way ANOVA (**f**), Two-tailed t-test (**a**, **c**, **d**). n.s.= not significant. Data are represented as mean ± SEM of biologically independent samples.

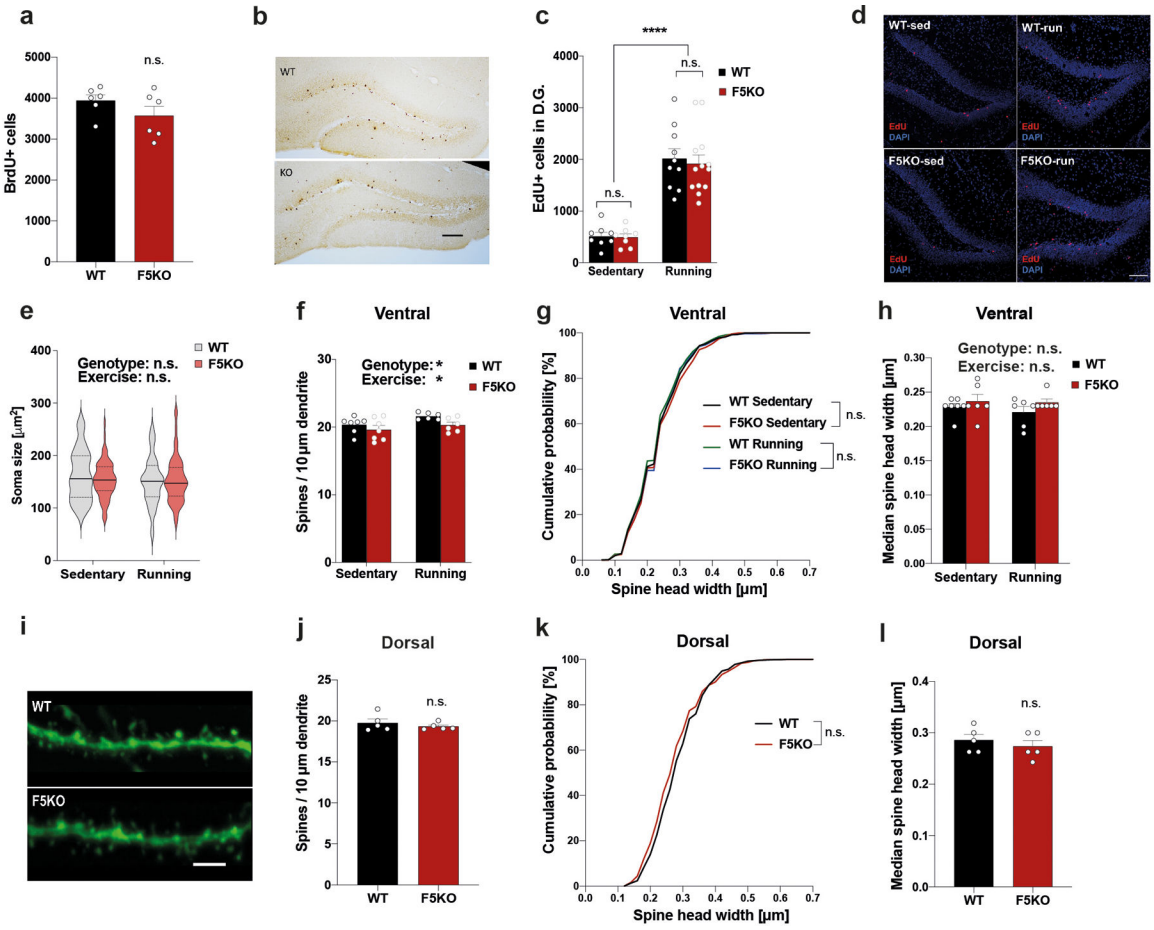

Extended Data Fig. 3: Adult-born neurons in the hippocampus are altered in global F5KO mice. **a and b,** Quantification (**a**) and representative immunohistochemistry images (**b**) of BrdU+ adult-borm hippocampal neurons in WT and F5KO mice (n = 6 per group). Scale bar 100 µm. **c and d,** Quantification (**c**) and representative immunofluorescence images (**d**) of EdU+ adult-born hippocampal neurons in WT and F5KO mice with or without running exercise (WT-sed n = 8, WT-run n = 10, F5KO n = 8, F5KO-run n = 13). Scale bar 100 µm. **e,** Soma size of adult-born hippocampal neurons (WT-sed n= 60, WT-run n = 60, F5KO-sed n = 65, F5KO-run n = 64 neurons). **f-h,** Dendritic spine analysis of newborn neurons in the ventral hippocampus. Dendritic spines density (**f**), cumulative distribution of spine head width (**g**), and median spine head width (**h**) (WT-sed n = 7, WT-run n = 6, F5KO-sed n = 7, F5KO-run n = 6 (**f**); WT-sed n = 1239, WT-run n = 1056, F5KO-sed n = 1089, F5KO-run n = 1047 spines (**g**); WT-sed n = 7, WT-run n = 6, F5KO-sed n = 6, F5KO-run n = 6 (**h**)). **i-l,** Dendritic spine analysis in mature granule cells in the dentate gyrus of *Thy1*-GFP/WT and *Thy1*-GFP/F5KO. Representative confocal images of dendritic spines stained with anti-GFP (green). Scale bar 5 µm (**i**), dendritic spines density (**j**), cumulative distribution of spine head width (**k**), and median spine head width (**l**) (n= 5 per group (**j, l**); WT n = 921, F5KO n = 948 spines (**k**)). Two-way ANOVA (**c**, **e**, **f, h**), Kruskal-Wallis ANOVA (**g**), Kolmogorov-Smirnov test (**k**), Two-tailed t-test (**a, j, l**). *p<0.05, ****p<0.0001, n.s.= not significant. Data are represented as mean ± SEM of biologically independent samples, except for violin

plots with center line = median, dotted line = upper and lower quartile (**e**). See source data for exact p-values.

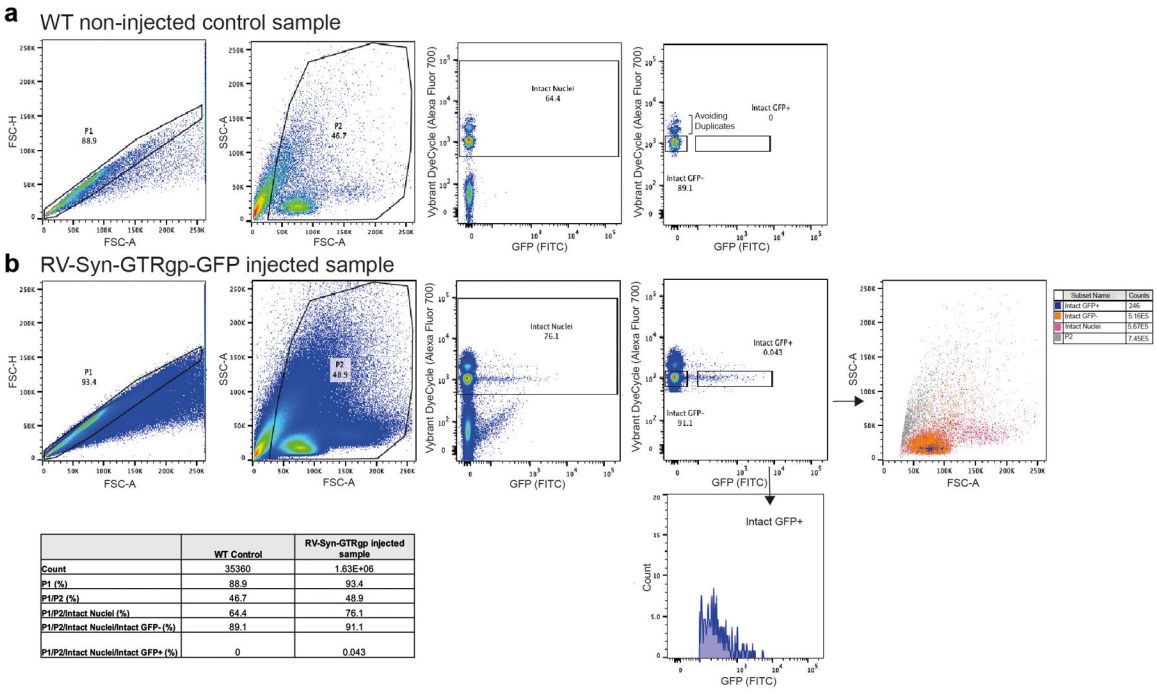

	WT Control	RV-Syn-GTRgp injected sample
Count	35360	1.63E+06
P1 (%)	88.9	93.4
P1/P2 (%)	46.7	48.9
P1/P2/Intact Nuclei (%)	64.4	76.1
P1/P2/Intact Nuclei/Intact GFP- (%)	89.1	91.1
P1/P2/Intact Nuclei/Intact GFP+ (%)	0	0.043

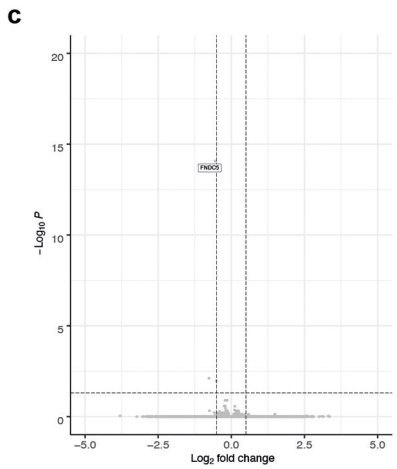

Extended Data Fig. 4: The transcriptome of adult-born neurons in the hippocampus is altered in global F5KO mice.

a and b, Representative FACS density plots of single nuclei isolated from the hippocampus of a non-injected WT control mouse (**a**) and a RV-Syn-GTRgp-GFP injected mouse (**b**). Nuclei were stained with Vybrant DyeCycle stain to label intact nuclei. **c,** Volcano plot of DESeq2 analysis of bulk RNA-sequencing of microdissected dentate gyrus from F5KO and WT mice (n= 5 per group).

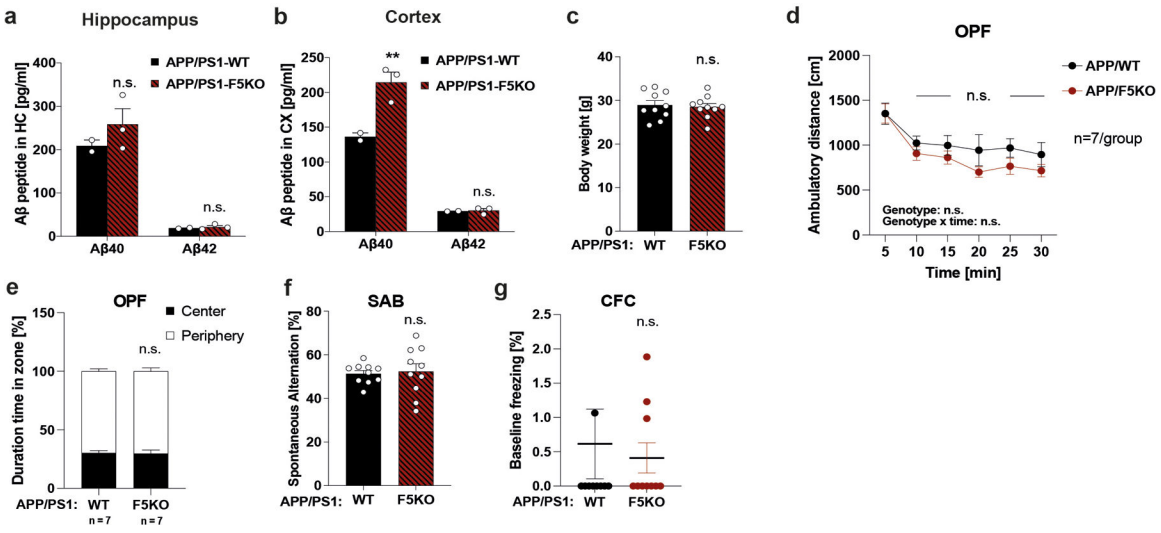

Extended Data Fig. 5: Genetic deletion of irisin impairs cognitive function in transgenic mouse models of AD.

a and b, MSD ELISA for Aβ−40 and Aβ−42 peptides in soluble fraction of hippocampus (**a**) and cortex (**b**) (APP/PS1-WT n = 2, APP/PS1-F5KO n = 3). **c**, Body weights at 6 months old. **d** and **e,** Open field test (OPF). **f**, Spontaneous Alternation Behavior (SAB). **g,** Baseline freezing in CFC. (n =10 per group (**c, f, g**); n= 7 per group (**d, e**)). RM-Two-way ANOVA (**d, e**), Two-way ANOVA (**a, b**), Two-tailed t-test (**c**, **f, g**). **p<0.01, n.s.= not significant. Data are represented as mean ± SEM of biologically independent samples. See source data for exact p-values.

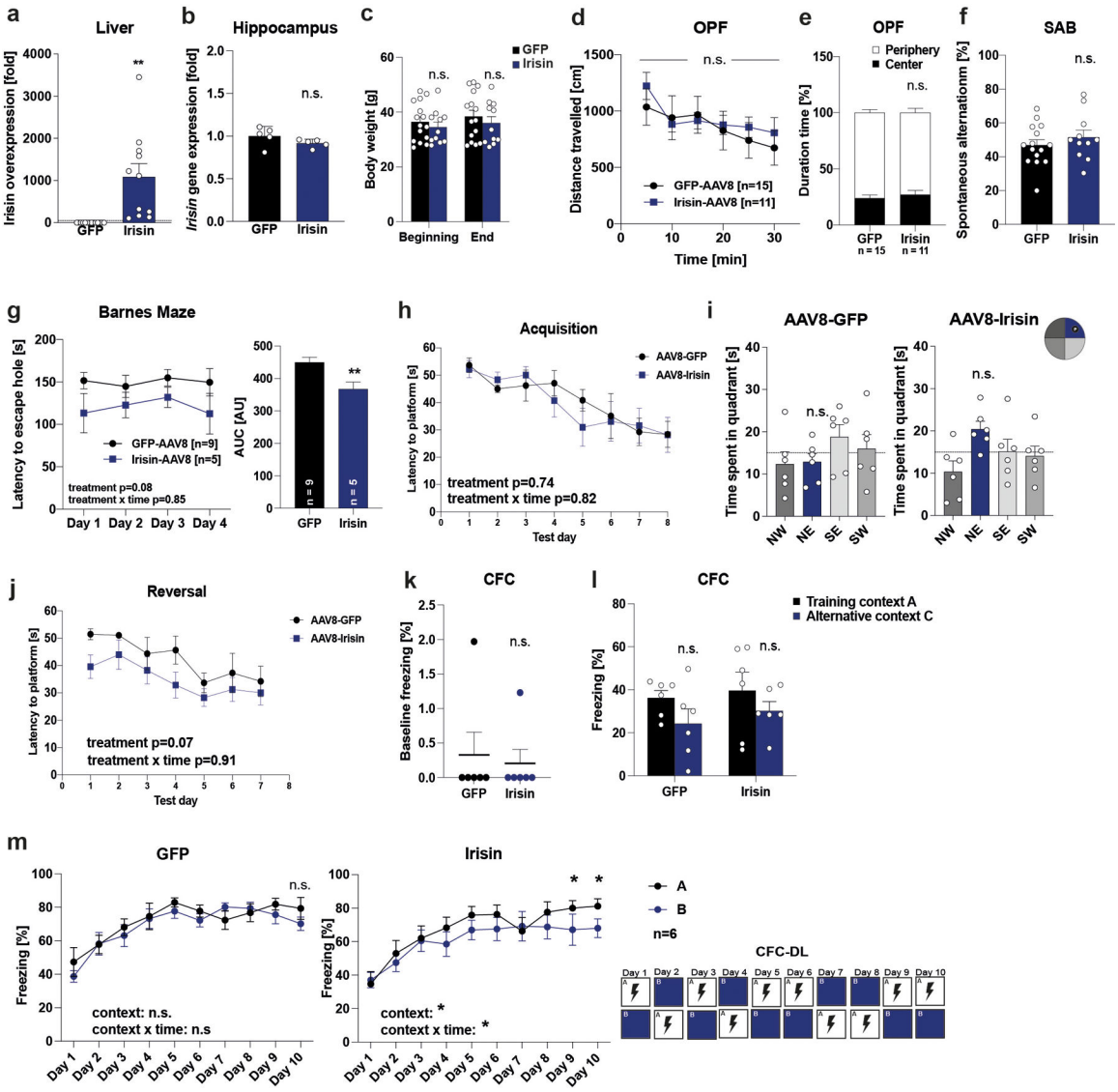

Extended Data Fig. 6: Peripheral irisin improves cognitive function in APP/PS1 transgenic mouse models of AD.

APP/PS1 mice were injected with AAV8-GFP or AAV8-irisin-FLAG via the tail vein. **a**, Liver (GFP n = 14, irisin n = 11) **b**, Hippocampus *Fndc5* mRNA expression (GFP n = 5, irisin n = 5), **c,** Bodyweights at the beginning and end of the experiment, **d and e,** OPF test, **f,** SAB (GFP n = 15, irisin n = 11). **g**, Barnes Maze, escape latency to hole (GFP n = 9, irisin n = 5), **h-j,** Morris-water-maze (MWM) latency to reach the target platform (**h**) and 24h probe trial in in acquisition **(i)**. SW quadrant (blue bar) was the target quadrant. Latency to reach the target platform in reversal (**j**) (GFP n = 6, irisin n = 6). **k and l,** Baseline freezing (**k**) and freezing in CFC (**l**), **m,** CFC-DL (n = 6 per group). RM-Two-way ANOVA (**c, d, e, g left, h, j, l, m**), One-way ANOVA followed by Fisher's LSD. Significance was assigned only if time spent in the target quadrant was significantly different from all other quadrants (**i**), Two-tailed t-test (**b, f, g right, k**), Two-tailed t-test with Welch's correction

(**a**). *p<0.05, **p<0.01, n.s.= not significant. Data are represented as mean ± SEM of biologically independent samples. See source data for exact p-values.

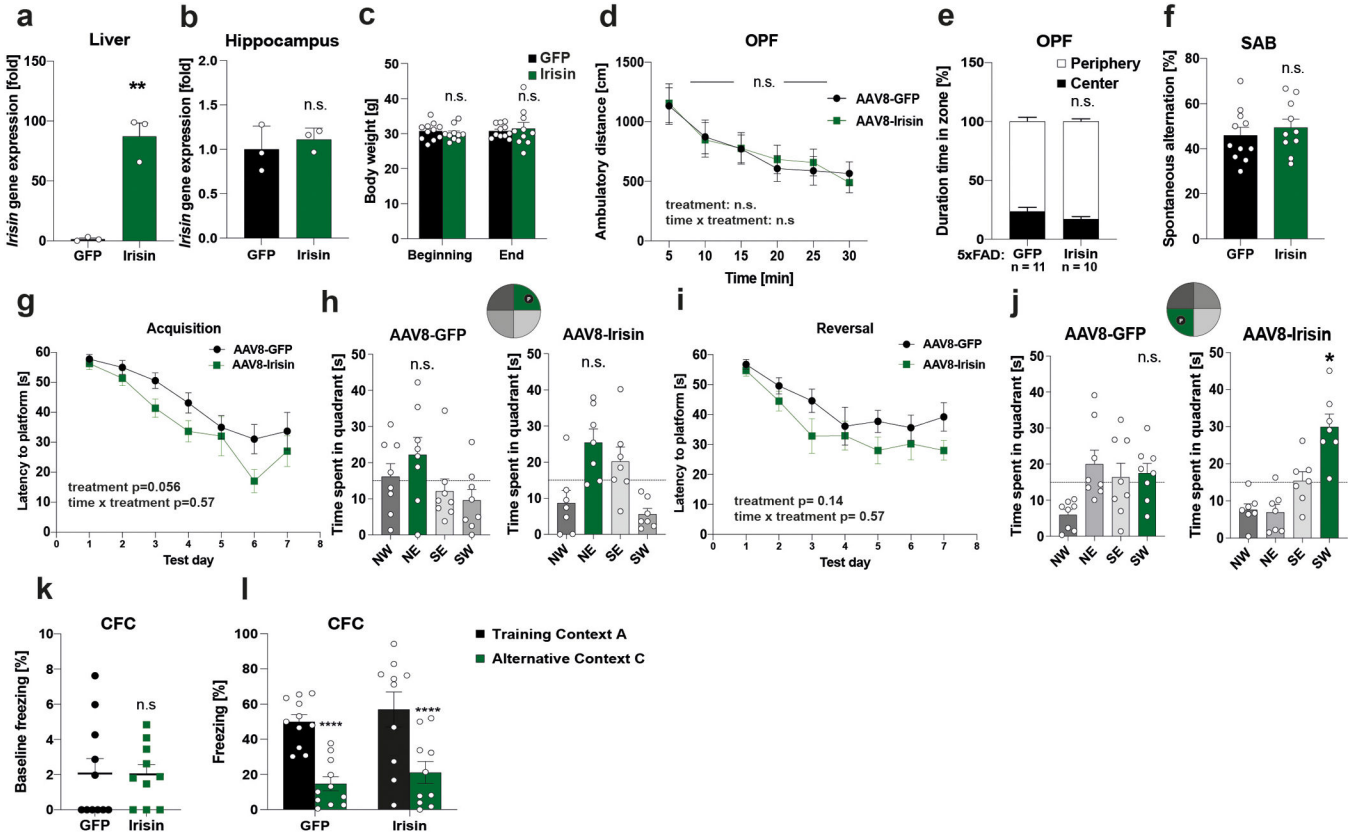

Extended Data Fig. 7: Peripheral irisin improves cognitive function in 5xFAD transgenic mouse models of AD.

5xFAD mice were injected with AAV8-GFP or AAV8-irisin-FLAG via the tail vein. **a,** Liver **b**, Hippocampus *Fndc5* mRNA expression (n=3 per group). **c,** Bodyweights at the beginning and end of the experiment, **d** and **e,** OPF test, **f,** SAB. **g-j,** Morris-water-maze (MWM) latency to reach the target platform in acquisition **(g)** and 24h probe trial in MWM in acquisition **(h)**. NE quadrant (green bar) was the target quadrant. Latency to reach the target platform in reversal (**i**) and 24h probe trial in MWM reversal (**j**). SW quadrant (green bar) was the target quadrant. **k and l,** CFC, baseline freezing (**k**) and freezing in CFC (**l**) (GFP n = 11, irisin n = 10 (**c-f, k, l**); GFP n = 8, irisin n = 7 (**g-j**)). RM-Two-way ANOVA (**c**, **d, e, g, i, l**), One-way ANOVA followed by Fisher's LSD. Significance was assigned only if time spent in the target quadrant was significantly different from all other quadrants (**h, j**), Two-tailed t-test (**a, b, f, k**). *p<0.05, **p<0.01, ****p<0.0001, n.s.= not significant, data are represented as mean ± SEM of biologically independent samples. See source data for exact p-values.

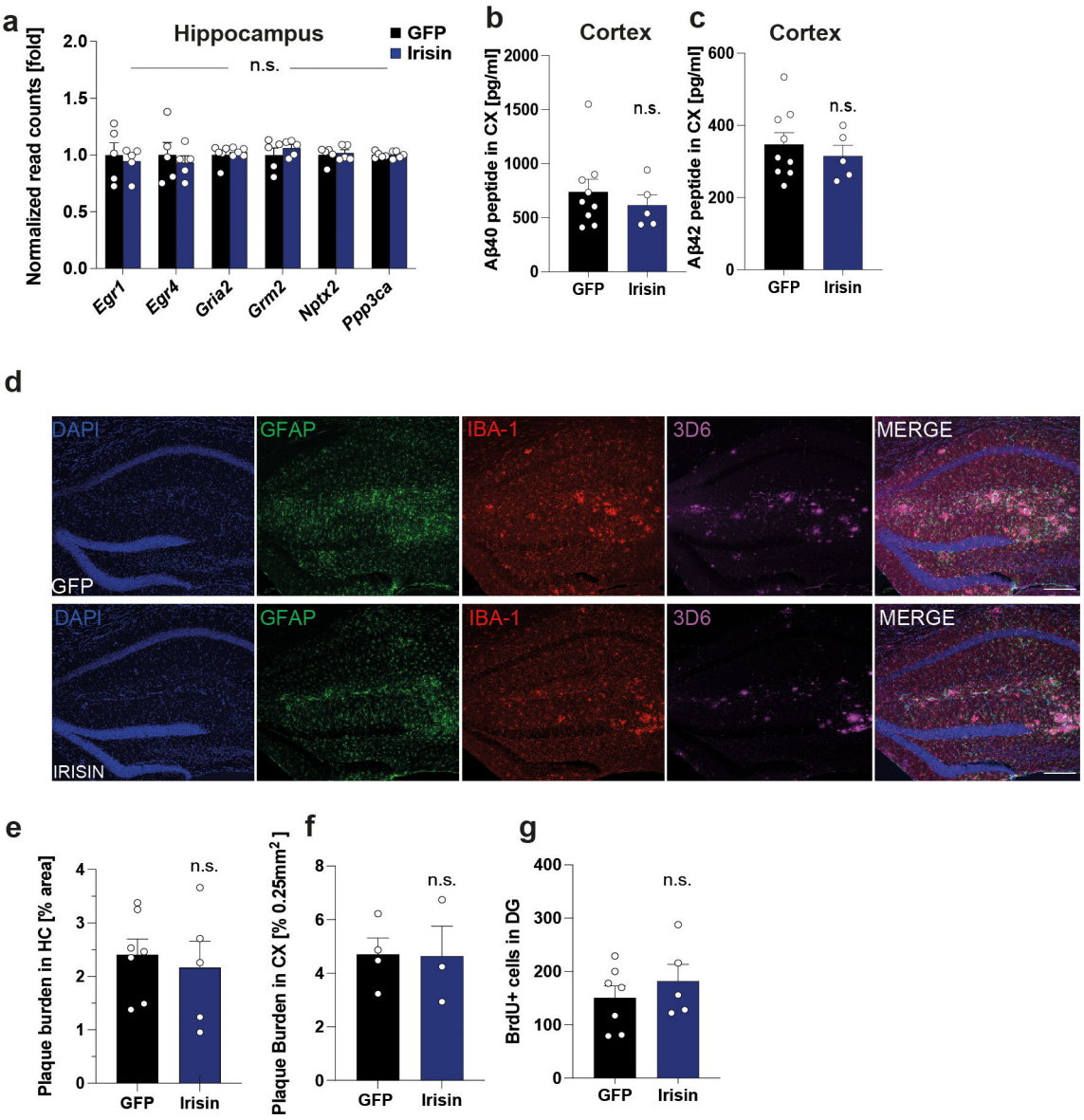

Extended Data Fig. 8: Peripheral irisin reduces glia activation in transgenic mouse models of AD.

APP/PS1 mice were injected with AAV8-GFP or AAV8-irisin-FLAG via the tail vein. **a,** Expression of synaptic plasticity genes in hippocampus derived from normalized read counts of RNA-seq analysis (GFP n = 5, irisin n = 5), **b**, MSD ELISA for Abeta40 peptide in cortex soluble fraction, **c,** MSD ELISA Abeta42 peptide in cortex soluble fraction (GFP n = 9, irisin n = 5). **d and e,** Representative immunofluorescence confocal images of hippocampus, GFAP (green), Iba-1 (red), 3D6 (Alexa 647). Scale bar 200 μm (**d**) and quantification of plaque burden in hippocampus (**e**) (GFP n = 7, irisin n =5). **f**, Quantification of plaque burden cortex (GFP n = 5, irisin n = 3). **g,** Quantification of total BrdU+ cells (GFP n = 7, irisin n = 5). Two-way ANOVA (**a**), Two-tailed t-test (**b, c, e-g**). n.s.= not significant, data are represented as mean ± SEM of biologically independent samples.

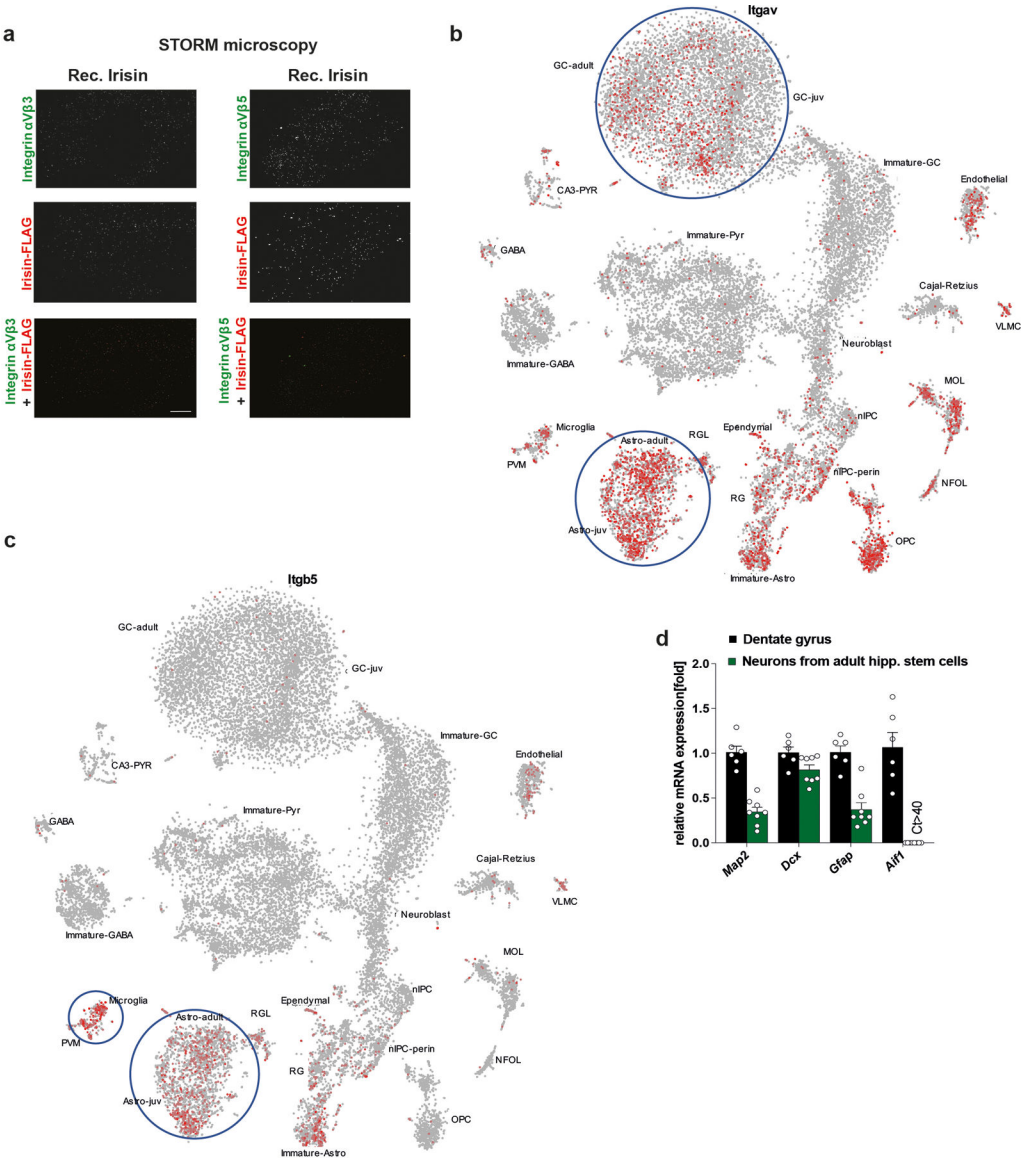

Extended Data Fig. 9: Irisin binds αV/β5 integrin receptor on astrocytes in adult hippocampal neural stem cells cultures.

a, Two-color dSTORM images of integrin αV/β3 (left) and αV/β5 (right) (green) and irisin-FLAG (red) molecules. Scale bar 5 μm (irisin-FLAG-αV/β3 n = 7, irisin-FLAG-αV/β5 n = 10), **b and c,** *Itgav* gene expression (**b**) and *Itgb5* gene expression (**c**) in the murine dentate gyrus from Linnarsson lab database (https://linnarssonlab.org/dentate/)[59]. **d,** QPCR analysis of mRNA expression of *Map2*, *Dcx*, *Gfap*, and *Aif1* in the dentate gyrus (n = 6) and neurons differentiated from adult hippocampal stem cells (n = 8 from two independent experiments). Ct: cycle threshold value. Data are represented as mean ± SEM of biologically independent samples.

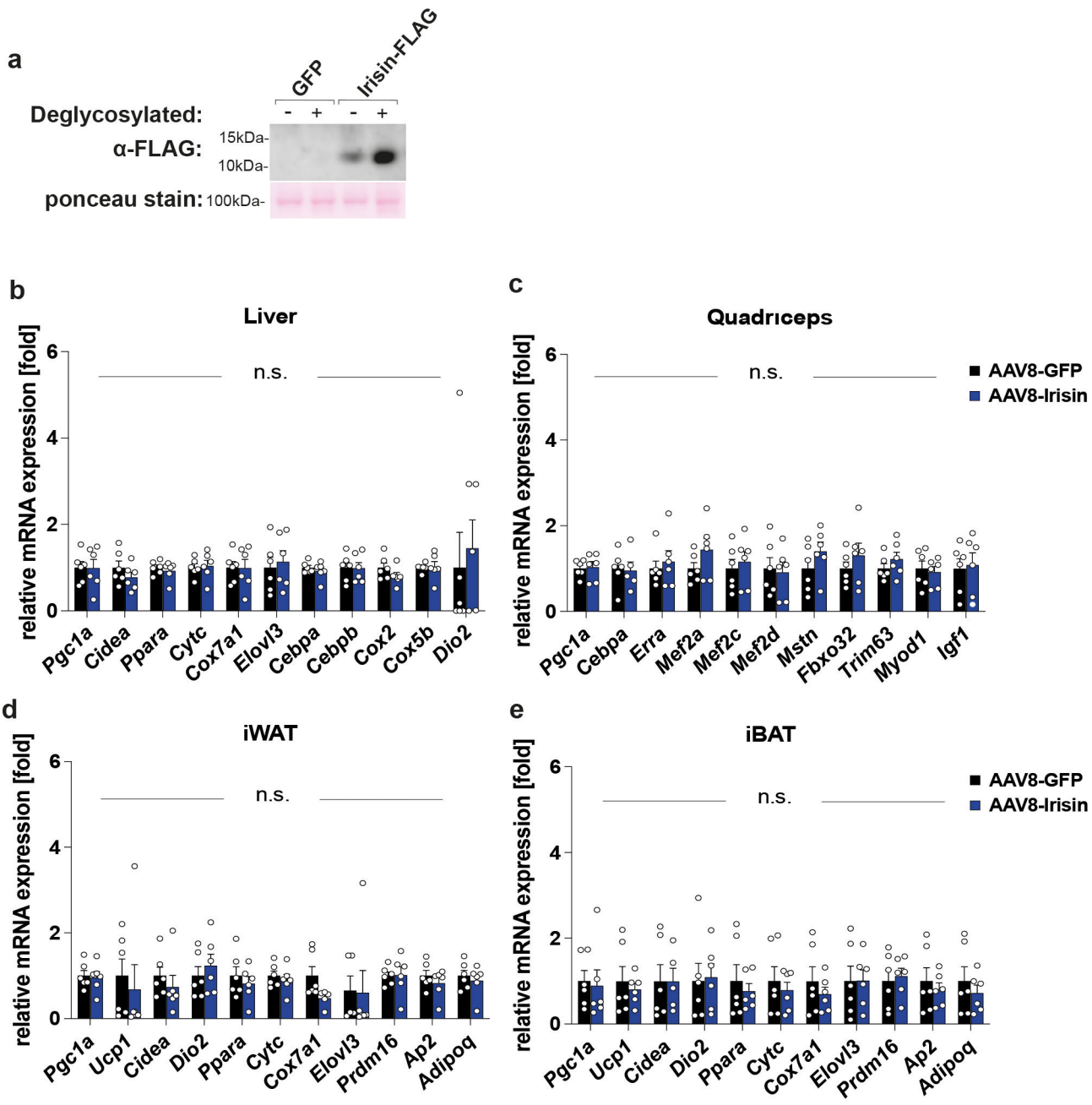

Extended Data Fig. 10: Peripherally delivered irisin has central effects.

a-e, WT mice injected with AAV8-GFP or AAV8-irisin-FLAG via the tail vein. Western blot of plasma from AAV8-GFP (1–2) and AAV8-irisin-FLAG (3–4) with or without deglycosylation (**a**), qPCR analysis of liver (**b**), quadriceps (**c**), inguinal white adipose tissue (iWAT) (**d**), interscapular brown adipose tissue (iBAT) (**e**). Two-way ANOVA (**b-d**). Data are represented as mean ± SEM of biologically independent samples (n = 6 per group) (**b-e**).

Supplementary Material

Refer to Web version on PubMed Central for supplementary material.

ACKNOWLEGMENTS

This work was supported by NIH grant no. NS087096 (C.D.W), AG062904 (C.D.W), AG064580 (C.D.W), 1R01AR065538 (R.J.S), 1R01CA193520 (R.J.S), R01DK062472 (R.J.S), S10RR027931 (R.J.S), K01DK089145 (A.B.S), R01DK062472 (A.B.S), the Cure Alzheimer's Fund (C.D.W, S.H. C., and R.E.T), an Alzheimer Association Research Grant (C.D.W), a SPARC Award from the McCance Center for Brain Health (C.D.W), the NeuroBehavior Laboratory Pilot Project Research Award from the Harvard NeuroDiscovery Center (C.D.W), the Hassenfeld Clinical Scholar Award (C.D.W), the Claflin Distinguished Scholar Award (C.D.W), the Harvard Brain Science Initiative Young Scientist Travel Award (M.R.I), the MSFHR (B.R.C. and L.E.B.B.), the FRAXA (B.R.C. and L.E.B.B.), the FXRFC (B.R.C. and L.E.B.B.), the NSERC (B.R.C. and L.E.B.B.), the CIHR (B.R.C. and L.E.B.B.), the JPB Foundation (B.M.S), and the MGH Molecular Imaging Core (R.J.S). We thank H. Van Praag for critical comments on the study design, data analysis, and the manuscript, and for providing us with the RV-CAG-GFP and RV-SYN-GTRgp. We acknowledge K. Gerber for technical assistance. We thank all members of the Wrann lab for helpful discussions. We thank Z. Herbert from the Molecular Biology Core Facilities at the Dana-Farber Cancer Institute for his support. We would like to acknowledge J. Long for help with designing the AAV8-irisin. We acknowledge the MGH Viral Vector Core (supported by NIH/NINDS P30NS04776) and the Penn Vector core for technical and instrument support. Schematic icons in Figures 4 and 5 were created with BioRender.com.

REFERENCES

1. Maass A et al. Vascular hippocampal plasticity after aerobic exercise in older adults. Mol Psychiatry 20, 585–593, doi:10.1038/mp.2014.114 (2015). [PubMed: 25311366]
2. Colcombe S & Kramer AF Fitness effects on the cognitive function of older adults: a meta-analytic study. Psychol Sci 14, 125–130 (2003). [PubMed: 12661673]
3. Voss MW et al. Exercise and Hippocampal Memory Systems. Trends Cogn Sci 23, 318–333, doi:10.1016/j.tics.2019.01.006 (2019). [PubMed: 30777641]
4. Buchman AS et al. Total daily physical activity and the risk of AD and cognitive decline in older adults. Neurology 78, 1323–1329, doi:10.1212/WNL.0b013e3182535d35 (2012). [PubMed: 22517108]
5. van Praag H, Christie BR, Sejnowski TJ & Gage FH Running enhances neurogenesis, learning, and long-term potentiation in mice. Proceedings of the National Academy of Sciences of the United States of America 96, 13427–13431 (1999). [PubMed: 10557337]
6. Choi SH et al. Combined adult neurogenesis and BDNF mimic exercise effects on cognition in an Alzheimer's mouse model. Science (New York, N.Y.) 361, doi:10.1126/science.aan8821 (2018).
7. Nichol KE et al. Exercise alters the immune profile in Tg2576 Alzheimer mice toward a response coincident with improved cognitive performance and decreased amyloid. Journal of neuroinflammation 5, 13, doi:10.1186/1742-2094-5-13 (2008). [PubMed: 18400101]
8. Bostrom P et al. A PGC1-alpha-dependent myokine that drives brown-fat-like development of white fat and thermogenesis. Nature 481, 463–468, doi:10.1038/nature10777 (2012). [PubMed: 22237023]
9. Wrann CD et al. Exercise induces hippocampal BDNF through a PGC-1alpha/FNDC5 pathway. Cell metabolism 18, 649–659, doi:10.1016/j.cmet.2013.09.008 (2013). [PubMed: 24120943]
10. Jedrychowski MP et al. Detection and Quantitation of Circulating Human Irisin by Tandem Mass Spectrometry. Cell metabolism 22, 734–740, doi:10.1016/j.cmet.2015.08.001 (2015). [PubMed: 26278051]
11. Kim H et al. Irisin Mediates Effects on Bone and Fat via alphaV Integrin Receptors. Cell 175, 1756–1768.e1717, doi:10.1016/j.cell.2018.10.025 (2018). [PubMed: 30550785]
12. Lourenco MV et al. Exercise-linked FNDC5/irisin rescues synaptic plasticity and memory defects in Alzheimer's models. Nature medicine 25, 165–175, doi:10.1038/s41591-018-0275-4 (2019).
13. Mustroph ML et al. Aerobic exercise is the critical variable in an enriched environment that increases hippocampal neurogenesis and water maze learning in male C57BL/6J mice. Neuroscience 219, 62–71, doi:10.1016/j.neuroscience.2012.06.007 (2012). [PubMed: 22698691]
14. Kobilo T et al. Running is the neurogenic and neurotrophic stimulus in environmental enrichment. Learning & memory (Cold Spring Harbor, N.Y.) 18, 605–609, doi:10.1101/lm.2283011 (2011).

15. Bolz L, Heigele S & Bischofberger J Running Improves Pattern Separation during Novel Object Recognition. Brain Plasticity 1, 129–141, doi:10.3233/BPL-150010 (2015). [PubMed: 29765837]
16. van Praag H, Shubert T, Zhao C & Gage FH Exercise enhances learning and hippocampal neurogenesis in aged mice. J Neurosci 25, 8680–8685, doi:10.1523/jneurosci.1731-05.2005 (2005). [PubMed: 16177036]
17. McNaughton BL, Barnes CA, Meltzer J & Sutherland RJ Hippocampal granule cells are necessary for normal spatial learning but not for spatially-selective pyramidal cell discharge. Experimental Brain Research 76, 485–496, doi:10.1007/BF00248904 (1989). [PubMed: 2792242]
18. Garthe A & Kempermann G An old test for new neurons: refining the Morris water maze to study the functional relevance of adult hippocampal neurogenesis. Frontiers in neuroscience 7, 63, doi:10.3389/fnins.2013.00063 (2013). [PubMed: 23653589]
19. McHugh TJ et al. Dentate Gyrus NMDA Receptors Mediate Rapid Pattern Separation in the Hippocampal Network. Science (New York, N.Y.) 317, 94–99, doi:10.1126/science.1140263 (2007). [PubMed: 17556551]
20. Hunsaker MR & Kesner RP Evaluating the differential roles of the dorsal dentate gyrus, dorsal CA3, and dorsal CA1 during a temporal ordering for spatial locations task. Hippocampus 18, 955–964, doi:10.1002/hipo.20455 (2008). [PubMed: 18493930]
21. Clelland CD et al. A functional role for adult hippocampal neurogenesis in spatial pattern separation. Science (New York, N.Y.) 325, 210–213, doi:10.1126/science.1173215 (2009). [PubMed: 19590004]
22. Creer DJ, Romberg C, Saksida LM, van Praag H & Bussey TJ Running enhances spatial pattern separation in mice. Proc Natl Acad Sci U S A 107, 2367–2372, doi:10.1073/pnas.0911725107 (2010). [PubMed: 20133882]
23. Ally BA, Hussey EP, Ko PC & Molitor RJ Pattern separation and pattern completion in Alzheimer's disease: evidence of rapid forgetting in amnestic mild cognitive impairment. Hippocampus 23, 1246–1258, doi:10.1002/hipo.22162 (2013). [PubMed: 23804525]
24. Déry N et al. Adult hippocampal neurogenesis reduces memory interference in humans: opposing effects of aerobic exercise and depression. Frontiers in neuroscience 7, 66, doi:10.3389/fnins.2013.00066 (2013). [PubMed: 23641193]
25. Sahay A et al. Increasing adult hippocampal neurogenesis is sufficient to improve pattern separation. Nature 472, 466–470, doi:10.1038/nature09817 (2011). [PubMed: 21460835]
26. Besnard A, Miller SM & Sahay A Distinct Dorsal and Ventral Hippocampal CA3 Outputs Govern Contextual Fear Discrimination. Cell reports 30, 2360–2373.e2365, doi:10.1016/j.celrep.2020.01.055 (2020). [PubMed: 32075769]
27. Rhodes JS, Garland T Jr. & Gammie SC Patterns of brain activity associated with variation in voluntary wheel-running behavior. Behavioral neuroscience 117, 1243–1256, doi:10.1037/0735-7044.117.6.1243 (2003). [PubMed: 14674844]
28. Oladehin A & Waters RS Location and distribution of Fos protein expression in rat hippocampus following acute moderate aerobic exercise. Exp Brain Res 137, 26–35, doi:10.1007/s002210000634 (2001). [PubMed: 11310169]
29. Sahay A, Wilson DA & Hen R Pattern separation: a common function for new neurons in hippocampus and olfactory bulb. Neuron 70, 582–588, doi:10.1016/j.neuron.2011.05.012 (2011). [PubMed: 21609817]
30. Aimone JB, Deng W & Gage FH Adult neurogenesis: integrating theories and separating functions. Trends Cogn Sci 14, 325–337, doi:10.1016/j.tics.2010.04.003 (2010). [PubMed: 20471301]
31. Colgin LL, Moser EI & Moser MB Understanding memory through hippocampal remapping. Trends in neurosciences 31, 469–477, doi:10.1016/j.tins.2008.06.008 (2008). [PubMed: 18687478]
32. Tapia-Rojas C, Aranguiz F, Varela-Nallar L & Inestrosa NC Voluntary Running Attenuates Memory Loss, Decreases Neuropathological Changes and Induces Neurogenesis in a Mouse Model of Alzheimer's Disease. Brain pathology (Zurich, Switzerland) 26, 62–74, doi:10.1111/bpa.12255 (2016). [PubMed: 25763997]

33. Moreno-Jiménez EP et al. Adult hippocampal neurogenesis is abundant in neurologically healthy subjects and drops sharply in patients with Alzheimer's disease. Nature medicine 25, 554–560, doi:10.1038/s41591-019-0375-9 (2019).
34. Spalding KL et al. Dynamics of hippocampal neurogenesis in adult humans. Cell 153, 1219–1227, doi:10.1016/j.cell.2013.05.002 (2013). [PubMed: 23746839]
35. Tobin MK et al. Human Hippocampal Neurogenesis Persists in Aged Adults and Alzheimer's Disease Patients. Cell stem cell 24, 974–982.e973, doi:10.1016/j.stem.2019.05.003 (2019). [PubMed: 31130513]
36. Mu Y & Gage FH Adult hippocampal neurogenesis and its role in Alzheimer's disease. Molecular neurodegeneration 6, 85, doi:10.1186/1750-1326-6-85 (2011). [PubMed: 22192775]
37. McAvoy KM et al. Modulating Neuronal Competition Dynamics in the Dentate Gyrus to Rejuvenate Aging Memory Circuits. Neuron 91, 1356–1373, doi:10.1016/j.neuron.2016.08.009 (2016). [PubMed: 27593178]
38. Zhao C, Jou J, Wolff LJ, Sun H & Gage FH Spine morphogenesis in newborn granule cells is differentially regulated in the outer and middle molecular layers. The Journal of comparative neurology 522, 2756–2766, doi:10.1002/cne.23581 (2014). [PubMed: 24610721]
39. Zhao C, Teng EM, Summers RG Jr., Ming GL & Gage FH Distinct morphological stages of dentate granule neuron maturation in the adult mouse hippocampus. J Neurosci 26, 3–11, doi:10.1523/jneurosci.3648-05.2006 (2006). [PubMed: 16399667]
40. Piatti VC et al. The timing for neuronal maturation in the adult hippocampus is modulated by local network activity. J Neurosci 31, 7715–7728, doi:10.1523/jneurosci.1380-11.2011 (2011). [PubMed: 21613484]
41. van Praag H et al. Functional neurogenesis in the adult hippocampus. Nature 415, 1030–1034, doi:10.1038/4151030a (2002). [PubMed: 11875571]
42. Goncalves JT et al. In vivo imaging of dendritic pruning in dentate granule cells. Nature neuroscience 19, 788–791, doi:10.1038/nn.4301 (2016). [PubMed: 27135217]
43. Anacker C et al. Hippocampal neurogenesis confers stress resilience by inhibiting the ventral dentate gyrus. Nature 559, 98–102, doi:10.1038/s41586-018-0262-4 (2018). [PubMed: 29950730]
44. Duman JG et al. The adhesion-GPCR BAI1 shapes dendritic arbors via Bcr-mediated RhoA activation causing late growth arrest. eLife 8, doi:10.7554/eLife.47566 (2019).
45. Saunders A et al. Molecular Diversity and Specializations among the Cells of the Adult Mouse Brain. Cell 174, 1015–1030.e1016, doi:10.1016/j.cell.2018.07.028 (2018). [PubMed: 30096299]
46. Vivar C et al. Monosynaptic inputs to new neurons in the dentate gyrus. Nature communications 3, 1107, doi:10.1038/ncomms2101 (2012).
47. Huang da W, Sherman BT & Lempicki RA Systematic and integrative analysis of large gene lists using DAVID bioinformatics resources. Nature protocols 4, 44–57, doi:10.1038/nprot.2008.211 (2009). [PubMed: 19131956]
48. Huang da W, Sherman BT & Lempicki RA Bioinformatics enrichment tools: paths toward the comprehensive functional analysis of large gene lists. Nucleic acids research 37, 1–13, doi:10.1093/nar/gkn923 (2009). [PubMed: 19033363]
49. Subramanian A et al. Gene set enrichment analysis: A knowledge-based approach for interpreting genome-wide expression profiles. Proceedings of the National Academy of Sciences 102, 15545, doi:10.1073/pnas.0506580102 (2005).
50. Mootha VK et al. PGC-1α-responsive genes involved in oxidative phosphorylation are coordinately downregulated in human diabetes. Nature genetics 34, 267–273, doi:10.1038/ng1180 (2003). [PubMed: 12808457]
51. Jankowsky JL et al. Mutant presenilins specifically elevate the levels of the 42 residue beta-amyloid peptide in vivo: evidence for augmentation of a 42-specific gamma secretase. Human molecular genetics 13, 159–170, doi:10.1093/hmg/ddh019 (2004). [PubMed: 14645205]
52. Fang EF et al. Mitophagy inhibits amyloid-β and tau pathology and reverses cognitive deficits in models of Alzheimer's disease. Nature neuroscience 22, 401–412, doi:10.1038/s41593-018-0332-9 (2019). [PubMed: 30742114]

53. Wan Y-W et al. Meta-Analysis of the Alzheimer's Disease Human Brain Transcriptome and Functional Dissection in Mouse Models. Cell reports 32, 107908, doi:10.1016/j.celrep.2020.107908 (2020). [PubMed: 32668255]
54. Haass C & Selkoe DJ Soluble protein oligomers in neurodegeneration: lessons from the Alzheimer's amyloid β-peptide. Nature Reviews Molecular Cell Biology 8, 101–112, doi:10.1038/nrm2101 (2007). [PubMed: 17245412]
55. Stakos DA et al. The Alzheimer's Disease Amyloid-Beta Hypothesis in Cardiovascular Aging and Disease: JACC Focus Seminar. Journal of the American College of Cardiology 75, 952–967, doi:10.1016/j.jacc.2019.12.033 (2020). [PubMed: 32130931]
56. Oakley H et al. Intraneuronal beta-amyloid aggregates, neurodegeneration, and neuron loss in transgenic mice with five familial Alzheimer's disease mutations: potential factors in amyloid plaque formation. J Neurosci 26, 10129–10140, doi:10.1523/jneurosci.1202-06.2006 (2006). [PubMed: 17021169]
57. Pluvinage JV & Wyss-Coray T Systemic factors as mediators of brain homeostasis, ageing and neurodegeneration. Nature reviews. Neuroscience 21, 93–102, doi:10.1038/s41583-019-0255-9 (2020). [PubMed: 31913356]
58. Leyns CEG & Holtzman DM Glial contributions to neurodegeneration in tauopathies. Molecular neurodegeneration 12, 50, doi:10.1186/s13024-017-0192-x (2017). [PubMed: 28662669]
59. Hochgerner H, Zeisel A, Lonnerberg P & Linnarsson S Conserved properties of dentate gyrus neurogenesis across postnatal development revealed by single-cell RNA sequencing. Nature neuroscience 21, 290–299, doi:10.1038/s41593-017-0056-2 (2018). [PubMed: 29335606]
60. Hong S et al. Complement and microglia mediate early synapse loss in Alzheimer mouse models. Science (New York, N.Y.) 352, 712–716, doi:10.1126/science.aad8373 (2016). [PubMed: 27033548]
61. Guo W et al. Ablation of Fmrp in adult neural stem cells disrupts hippocampus-dependent learning. Nat Med 17, 559–565, doi:10.1038/nm.2336 (2011). [PubMed: 21516088]
62. Guo W, Patzlaff NE, Jobe EM & Zhao X Isolation of multipotent neural stem or progenitor cells from both the dentate gyrus and subventricular zone of a single adult mouse. Nat Protoc 7, 2005–2012, doi:10.1038/nprot.2012.123 (2012). [PubMed: 23080272]
63. Sah N, Peterson BD, Lubejko ST, Vivar C & van Praag H Running reorganizes the circuitry of one-week-old adult-born hippocampal neurons. Scientific Reports 7, 10903, doi:10.1038/s41598-017-11268-z (2017). [PubMed: 28883658]
64. Nuber S et al. Abrogating Native α-Synuclein Tetramers in Mice Causes a L-DOPA-Responsive Motor Syndrome Closely Resembling Parkinson's Disease. Neuron 100, 75–90.e75, doi:10.1016/j.neuron.2018.09.014 (2018). [PubMed: 30308173]
65. Liu B et al. Space-like (56)Fe irradiation manifests mild, early sex-specific behavioral and neuropathological changes in wildtype and Alzheimer's-like transgenic mice. Sci Rep 9, 12118, doi:10.1038/s41598-019-48615-1 (2019). [PubMed: 31431669]
66. Caldarone BJ et al. The novel triple reuptake inhibitor JZAD-IV-22 exhibits an antidepressant pharmacological profile without locomotor stimulant or sensitization properties. The Journal of pharmacology and experimental therapeutics 335, 762–770, doi:10.1124/jpet.110.174011 (2010). [PubMed: 20864506]
67. Shi Q et al. Complement C3-Deficient Mice Fail to Display Age-Related Hippocampal Decline. J Neurosci 35, 13029–13042, doi:10.1523/jneurosci.1698-15.2015 (2015). [PubMed: 26400934]
68. Morris R Developments of a water-maze procedure for studying spatial learning in the rat. J Neurosci Methods 11, 47–60, doi:10.1016/0165-0270(84)90007-4 (1984). [PubMed: 6471907]
69. Vorhees CV & Williams MT Morris water maze: procedures for assessing spatial and related forms of learning and memory. Nature protocols 1, 848–858, doi:10.1038/nprot.2006.116 (2006). [PubMed: 17406317]
70. Leger M et al. Object recognition test in mice. Nature Protocols 8, 2531–2537, doi:10.1038/nprot.2013.155 (2013). [PubMed: 24263092]
71. Wolf A, Bauer B, Abner EL, Ashkenazy-Frolinger T & Hartz AM A Comprehensive Behavioral Test Battery to Assess Learning and Memory in 129S6/Tg2576 Mice. PloS one 11, e0147733, doi:10.1371/journal.pone.0147733 (2016). [PubMed: 26808326]

72. Faizi M et al. Thy1-hAPP(Lond/Swe+) mouse model of Alzheimer's disease displays broad behavioral deficits in sensorimotor, cognitive and social function. Brain and behavior 2, 142–154, doi:10.1002/brb3.41 (2012). [PubMed: 22574282]

73. Zhao X & van Praag H Steps towards standardized quantification of adult neurogenesis. Nature communications 11, 4275, doi:10.1038/s41467-020-18046-y (2020).

74. Young K & Morrison H Quantifying Microglia Morphology from Photomicrographs of Immunohistochemistry Prepared Tissue Using ImageJ. J Vis Exp, doi:10.3791/57648 (2018).

75. Fontaine CJ et al. Impaired Bidirectional Synaptic Plasticity in Juvenile Offspring Following Prenatal Ethanol Exposure. Alcohol Clin Exp Res 43, 2153–2166, doi:10.1111/acer.14170 (2019). [PubMed: 31386206]

76. Peñasco S et al. Endocannabinoid long-term depression revealed at medial perforant path excitatory synapses in the dentate gyrus. Neuropharmacology 153, 32–40, doi:10.1016/j.neuropharm.2019.04.020 (2019). [PubMed: 31022405]

77. Schmittgen TD & Livak KJ Analyzing real-time PCR data by the comparative C(T) method. Nat Protoc 3, 1101–1108 (2008). [PubMed: 18546601]

78. Schmider AB et al. Two- and three-color STORM analysis reveals higher-order assembly of leukotriene synthetic complexes on the nuclear envelope of murine neutrophils. The Journal of biological chemistry 295, 5761–5770, doi:10.1074/jbc.RA119.012069 (2020). [PubMed: 32152223]

79. Bilsland JG et al. Behavioral and Neurochemical Alterations in Mice Deficient in Anaplastic Lymphoma Kinase Suggest Therapeutic Potential for Psychiatric Indications. Neuropsychopharmacology 33, 685–700, doi:10.1038/sj.npp.1301446 (2008). [PubMed: 17487225]

80. Kim WB & Cho J-H Encoding of contextual fear memory in hippocampal–amygdala circuit. Nature Communications 11, 1382, doi:10.1038/s41467-020-15121-2 (2020).

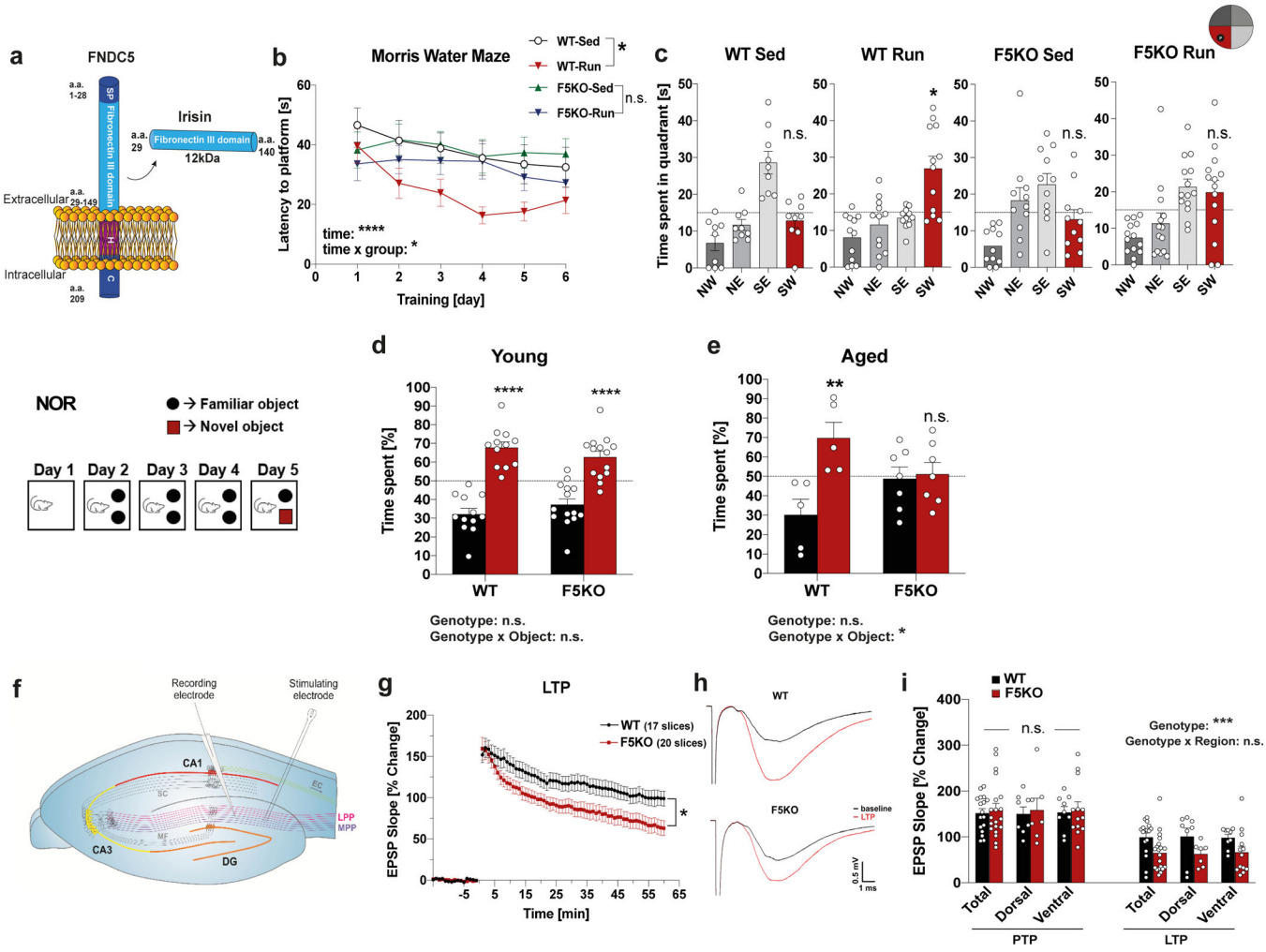

Fig. 1. Genetic deletion of irisin impairs cognitive function in exercise and aging.

a, Schematic representation of FNDC5 and irisin. SP= signal peptide, H= hydrophobic domain, C=c-terminal domain a.a.= amino acid. **b and c**, Morris-water-maze (MWM) latency to reach the target platform in reversal (**b**) (WT-sed n = 9, WT-run n = 12, F5KO-sed n = 12, F5KO-run n = 14) and 24h probe trial in MWM in reversal (**c**). SW quadrant (red bar) was the target quadrant (WT-sed n = 9, WT-run n = 12, F5KO-sed n = 11, F5KO-run n = 14). **d and e,** Novel object recognition (NOR) task in young (**d**) (WT n = 12, F5KO n = 14) and aged mice (**e**) (WT n = 5, F5KO n = 7). **f-i,** Electrophysiology of WT and F5KO using acute hippocampal slices. Schematic showing electrode position to evoke field EPSPs in the dentate gyrus (**f**), EPSP recordings for LTP measurement (55–60 min after application of a conditioning stimulus, two-tailed t-test on the average from last five minutes) (**g**), representative traces indicating the average LTP elicited (**h**), and EPSP slope change in different subregions of hippocampus in the PTP (first minute after conditioning stimulus) and LTP phase (55–60 min after induction) (**i**) (WT n = 17, F5KO n = 20 slices (**g**); WT-Total n = 17, WT-dorsal n = 8, WT-ventral n = 9, F5KO-Total n = 20, F5KO-dorsal n = 7, F5KO-ventral n = 13 slices (**i**), from 7 animals per group). RM-Two-way ANOVA (**b**), Two-way ANOVA (**d, e, i**). One-way ANOVA followed by Fisher's LSD. Significance was

assigned only if time spent in the target quadrant was significantly different from all other quadrants (**c**), Two-tailed t-test (**g**). *p<0.05, **p<0.01, ***p<0.001, ****p<0.0001. n.s.= not significant. Data represented as mean ± SEM of biologically independent samples. See source data for exact p-values.

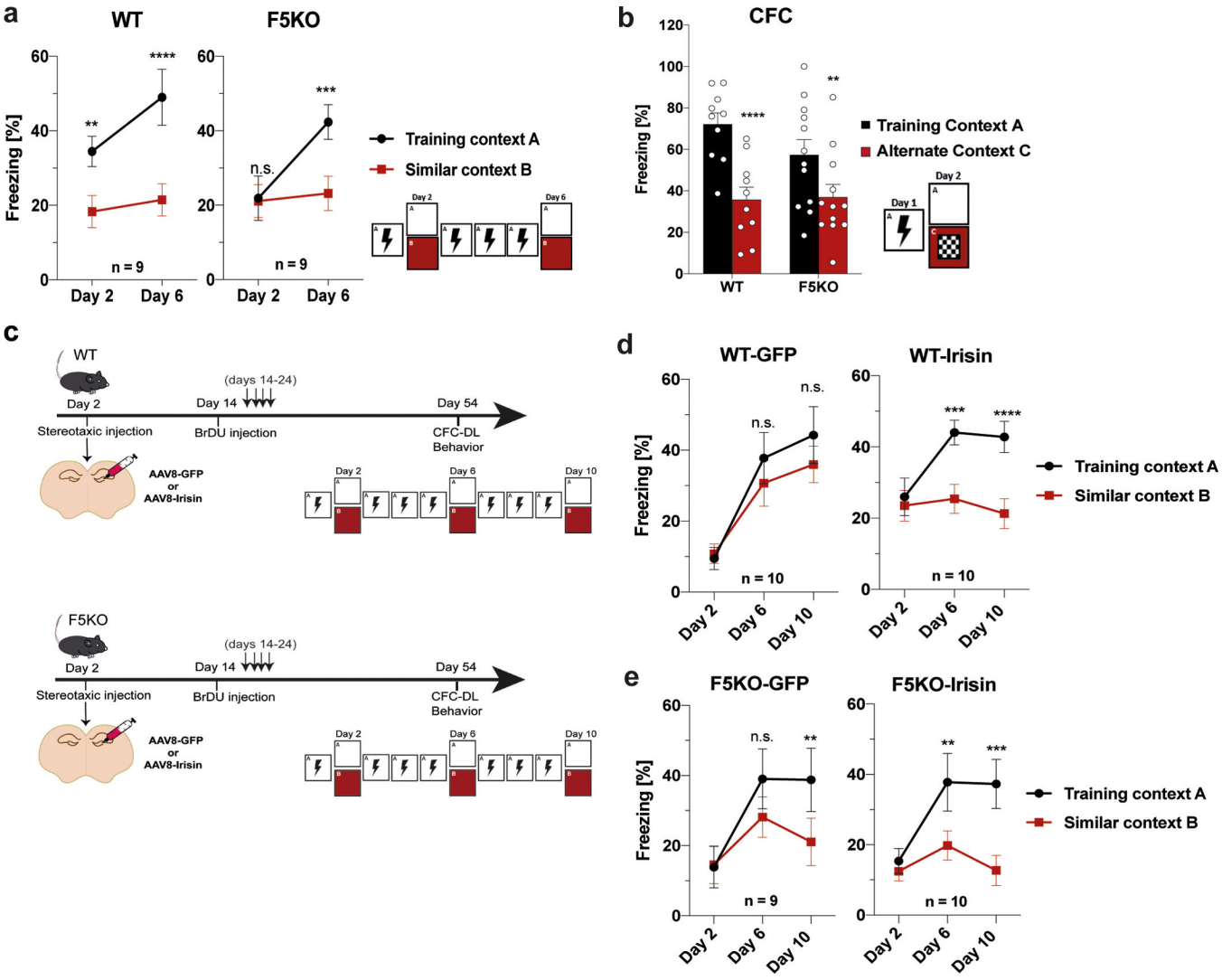

Fig. 2. Pattern separation is impaired in F5KO mice and can be rescued by delivering irisin directly into the dentate gyrus.

a, Contextual fear conditioning discrimination learning paradigm (CFC-DL) for WT and F5KO mice (n = 9 per group). **b**, Contextual fear conditioning (CFC) for WT and F5KO mice (WT n = 10, F5KO n = 12), **c-e**, WT and F5KO were stereotaxically injected with AAV8-GFP or AAV8-irisin-FLAG into the dentate gyrus. Schematic of experimental layout (**c**), CFC-DL of AAV8-GFP or AAV8-irisin injected WT (**d**) and F5KO mice (**e**) (WT-GFP n = 10, WT-irisin n = 10, F5KO-GFP n = 9, F5KO-irisin n = 10). RM-Two-way ANOVA (**a, b, d, e**). **p<0.01, ***p<0.001, ****p<0.0001. n.s.= not significant. Data represented as mean ± SEM of biologically independent samples. See source data for exact p-values.

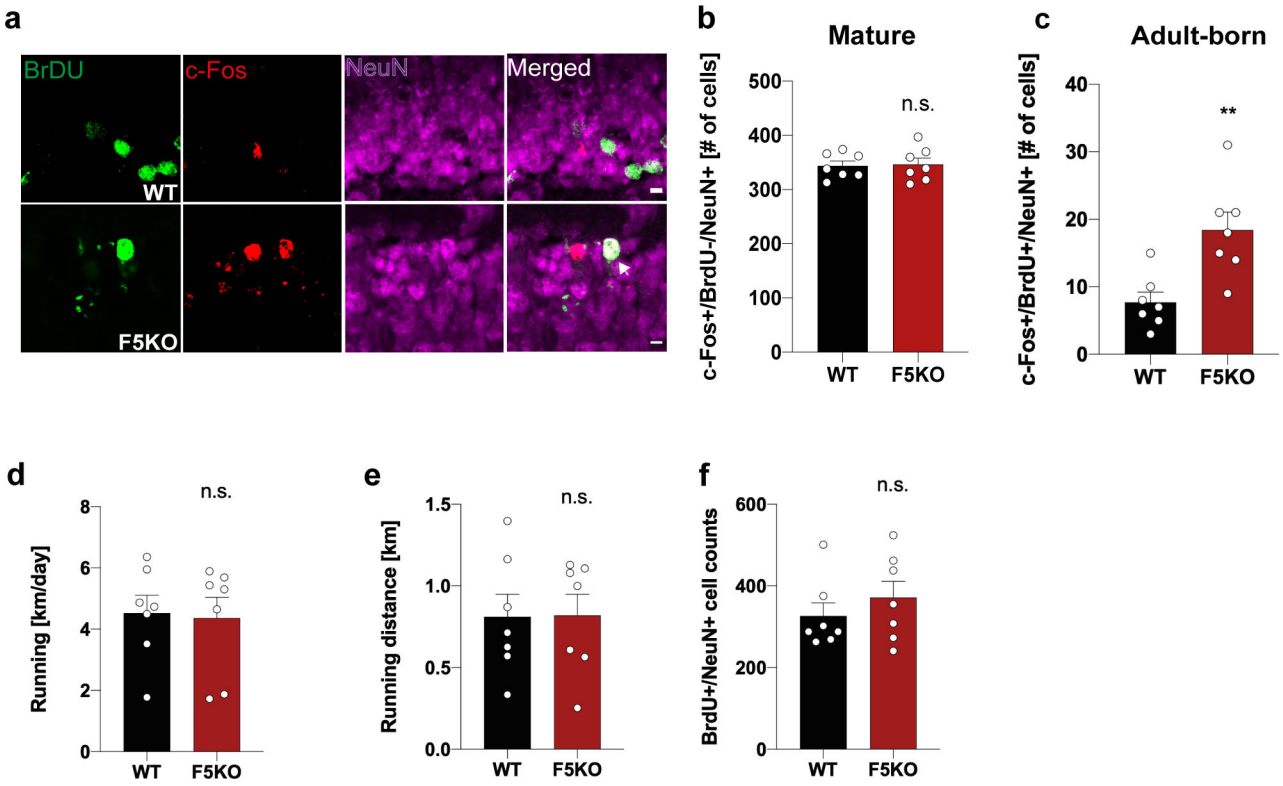

Fig. 3. Adult-born neurons, but not mature granule cells, in the hippocampus display aberrant activation in global F5KO mice.

a-c, Representative confocal images of the dentate gyrus stained with anti-BrdU (green), c-Fos (red), and Neun (magenta), white arrowhead indicates triple-positive cell. Scale bar 5 μm (**a**) and quantification of BrdU-, c-Fos+, NeuN+ mature granule cells (**b**) and BrdU+, c-Fos+, NeuN+ adult-born neurons (**c**) in the dentate gyrus from WT and F5KO mice. **d,** Running activity/day. **e,** Total running ninety minutes before sacrificing the mouse. **f**, Total number of BrdU+/NeuN+ cells (n = 7 per group). Two-tailed t-test (**b-f**). **p<0.01, n.s.= not significant. Data represented as mean ± SEM of biologically independent samples. See source data for exact p-values.

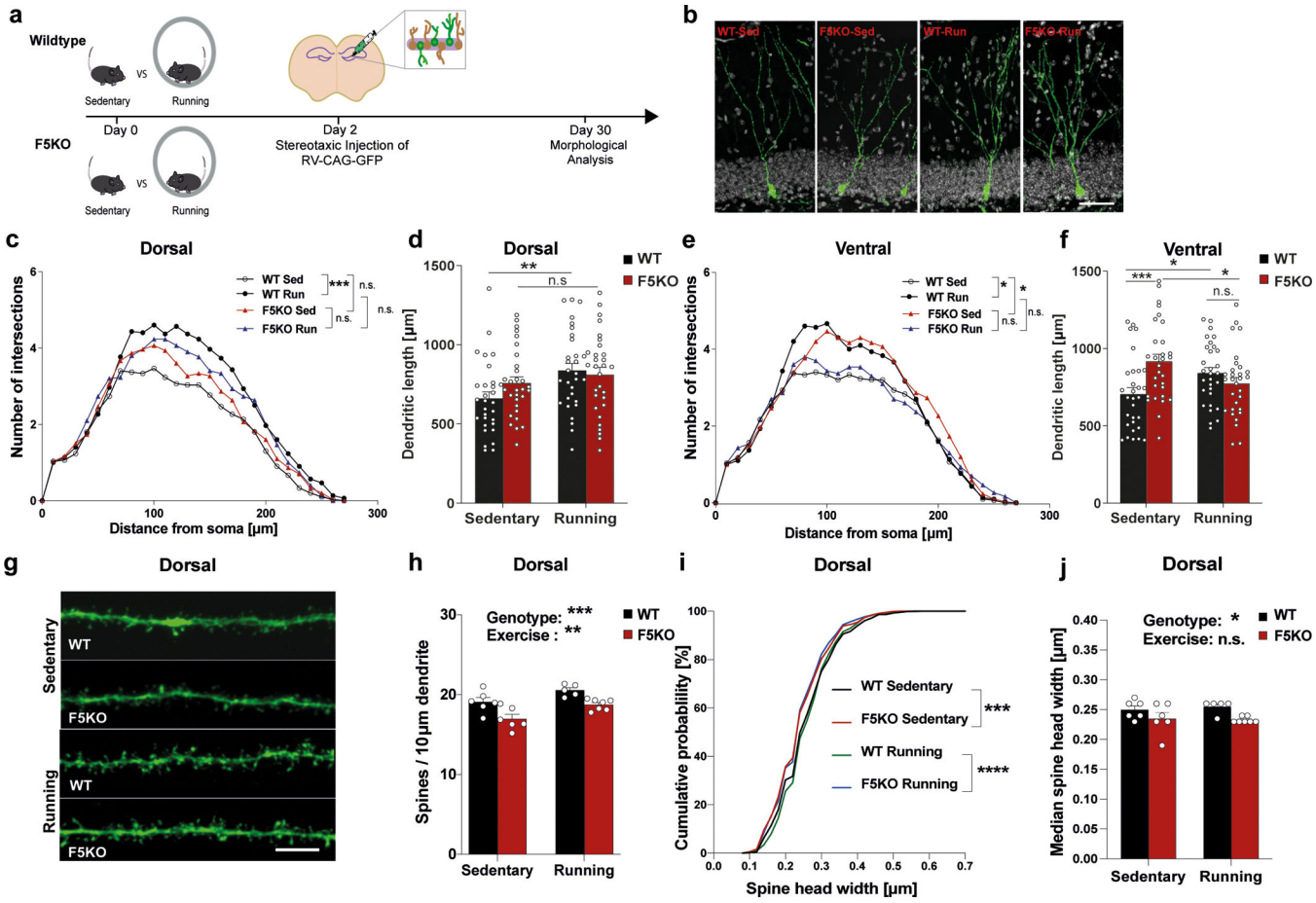

Fig. 4. Adult-born neurons in the hippocampus develop abnormally in global F5KO mice.

a, Schematic of CAG-GFP retrovirus injection to label newborn neurons in the hippocampus. **b-f,** Morphological analysis of dendrites of newborn neurons. Representative confocal images of newborn neurons stained with anti-GFP (green) and DAPI (white). Scale bar 100 µm (**b**), Sholl analysis of dendritic complexity (**c**), and total dendritic length of newborn neurons in the dorsal hippocampus (**d**), and Sholl analysis of dendritic complexity (**e**) and total dendritic length of newborn neurons in the ventral hippocampus (**f**) (n=30 neurons per group). **g-j,** Dendritic spine analysis in dorsal newborn neurons. Representative confocal images of dendritic spines stained with anti-GFP (green). Scale bar 5 µm (**g**), dendritic spines density (**h**), cumulative distribution of spine head width (**i**), and median spine head width (**j**) (WT-sed, n = 6, WT-run, n = 5, F5KO-sed, n = 6, F5KO-run, n = 7 (**h, j**)); (WT-sed, n = 966, WT-run, n = 817, F5KO-sed, n = 1018, F5KO-run, n = 1180 spines, (**i**)). RM-Two-way ANOVA (**c, e**). Two-way ANOVA (**d, f, h, j**), Kruskal-Wallis ANOVA test (**i**). *p<0.05, **p<0.01, ***p<0.001, ****p<0.0001, n.s.= not significant. Data represented as mean ± SEM of biologically independent samples, except for violin plots with center line=median, dotted line= upper and lower quartile (**d**, **f**). See source data for exact p-values.

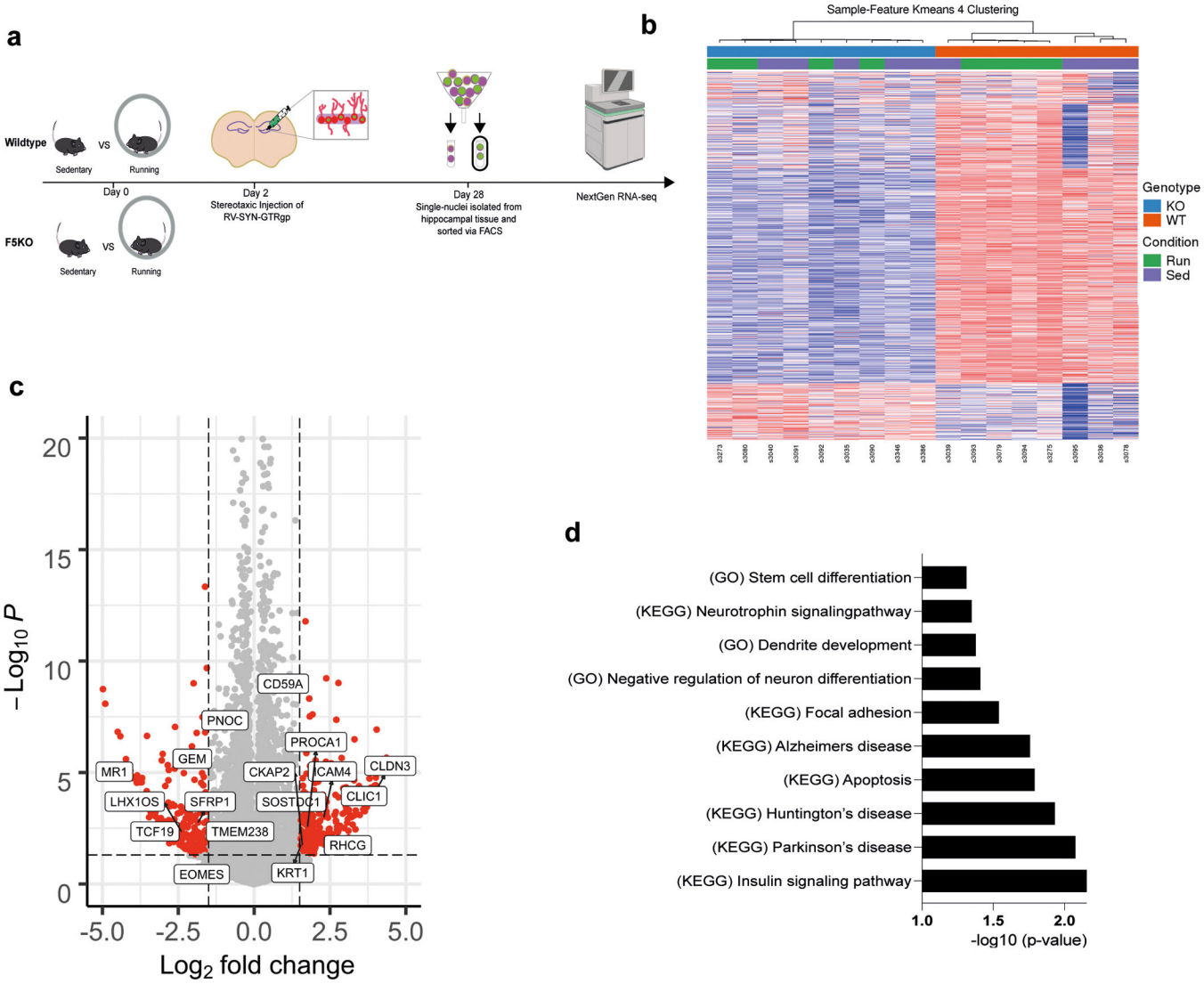

Fig. 5. The transcriptome of adult-born neurons in the hippocampus is altered in global F5KO mice.

a, Schematic of selective labeling and FACS sorting of single nuclei of newborn neurons for transcriptomic analysis by RNA-seq. **b,** Heatmap of Sample-Feature K-means 4 Clustering (blue: F5KO, red: WT, green: Run, purple: Sed). **c,** Volcano plot of DESeq2 analysis and **d,** GSEA analysis for dysregulated pathways in newborn neurons in F5KO (WT-sed n = 4, WT-run n = 4, F5KO-run n=4, F5KO-sed n = 5). See source data for exact p-values.

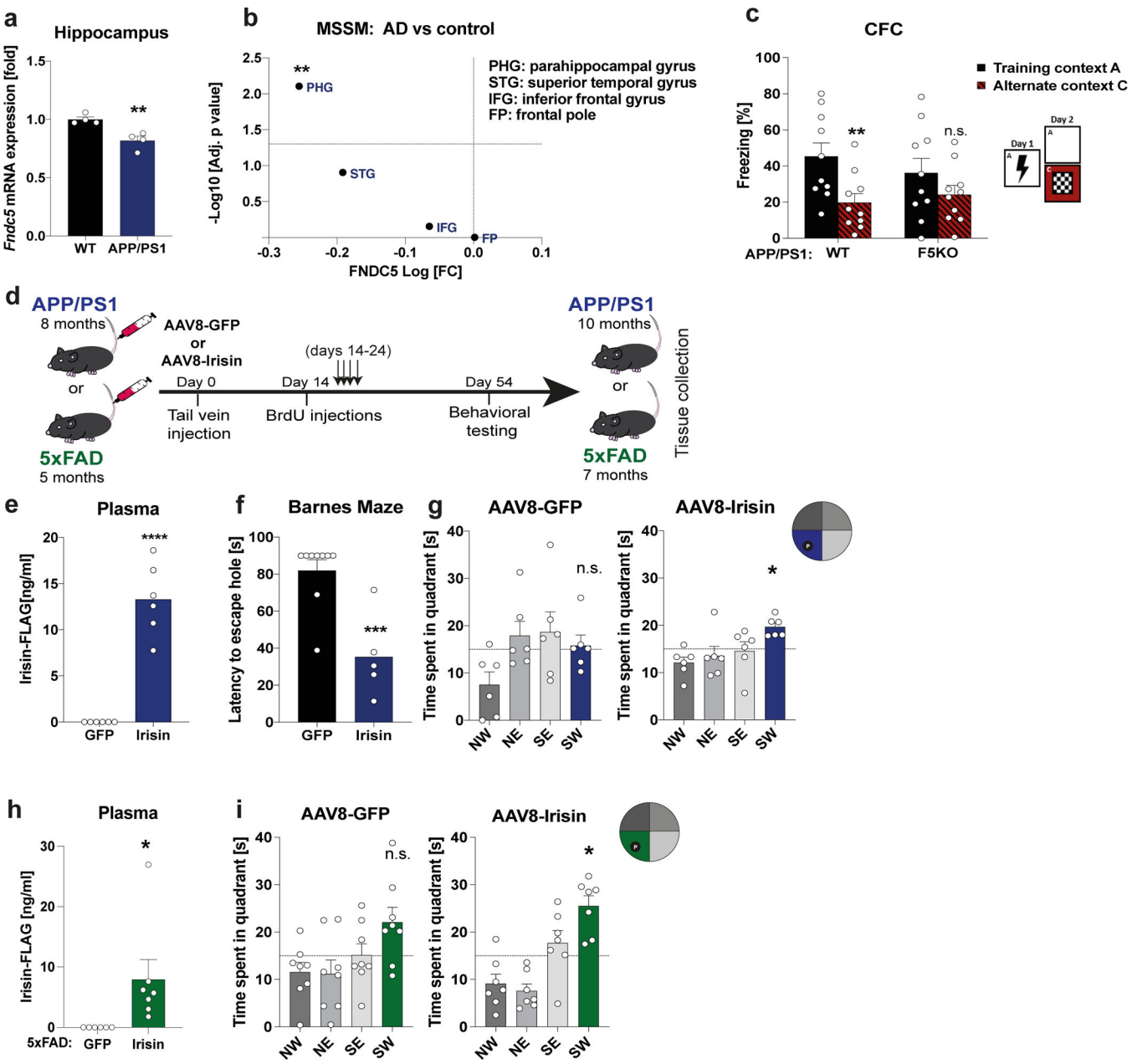

Fig. 6. Peripheral irisin improves cognitive function in transgenic mouse models of AD.

a, Hippocampal *Fndc5* mRNA expression in WT and APP/PS1 AD mice (n = 4 per group). **b,** FNDC5 mRNA expression from RNA-sequencing data from the MSSM study (Mount Sinai School of Medicine, and Mayo), comprising 2,114 samples from 1,234 subjects. **c,** Contextual fear conditioning (CFC) in APP/PS1-WT (n = 10) and APP/PS1-F5KO mice (n = 10). **d,** Schematic of experimental outline for irisin-treatment of transgenic AD models. **e-g,** APP/PS1 mice were injected with AAV8-GFP or AAV8-irisin-FLAG via the tail vein. Irisin-FLAG level in the plasma by ELISA (**e**) (n = 6 per group), escape latency in the probe trial in the Barnes maze (**f**) (GFP n = 9, irisin n = 5), and 4h probe trial in the MWM reversal. SW quadrant (blue bar) was the target quadrant (n = 6 per group)

(**g**). **h and i,** 5xFAD mice were injected with AAV8-GFP or AAV8-irisin-FLAG via the tail vein. Irisin-FLAG levels in the plasma by ELISA (GFP n = 6, irisin n = 7) (**h**), and 4h probe trial in MWM reversal. SW quadrant (green bar) was the target quadrant (GFP n = 8, irisin n = 7) (**i**). RM-Two-way ANOVA (**c**), One-way ANOVA followed by Fisher's LSD. Significance was assigned only if time spent in the target quadrant was significantly different from all other quadrants (**g, i**), Two-tailed t-test (**a, b**, **e**, **f**, **h**). *****p<0.05, **p<0.01, ***p<0.001, ****p<0.0001; n.s.= not significant. Data presented as mean ± SEM of biologically independent samples. See source data for exact p-values.

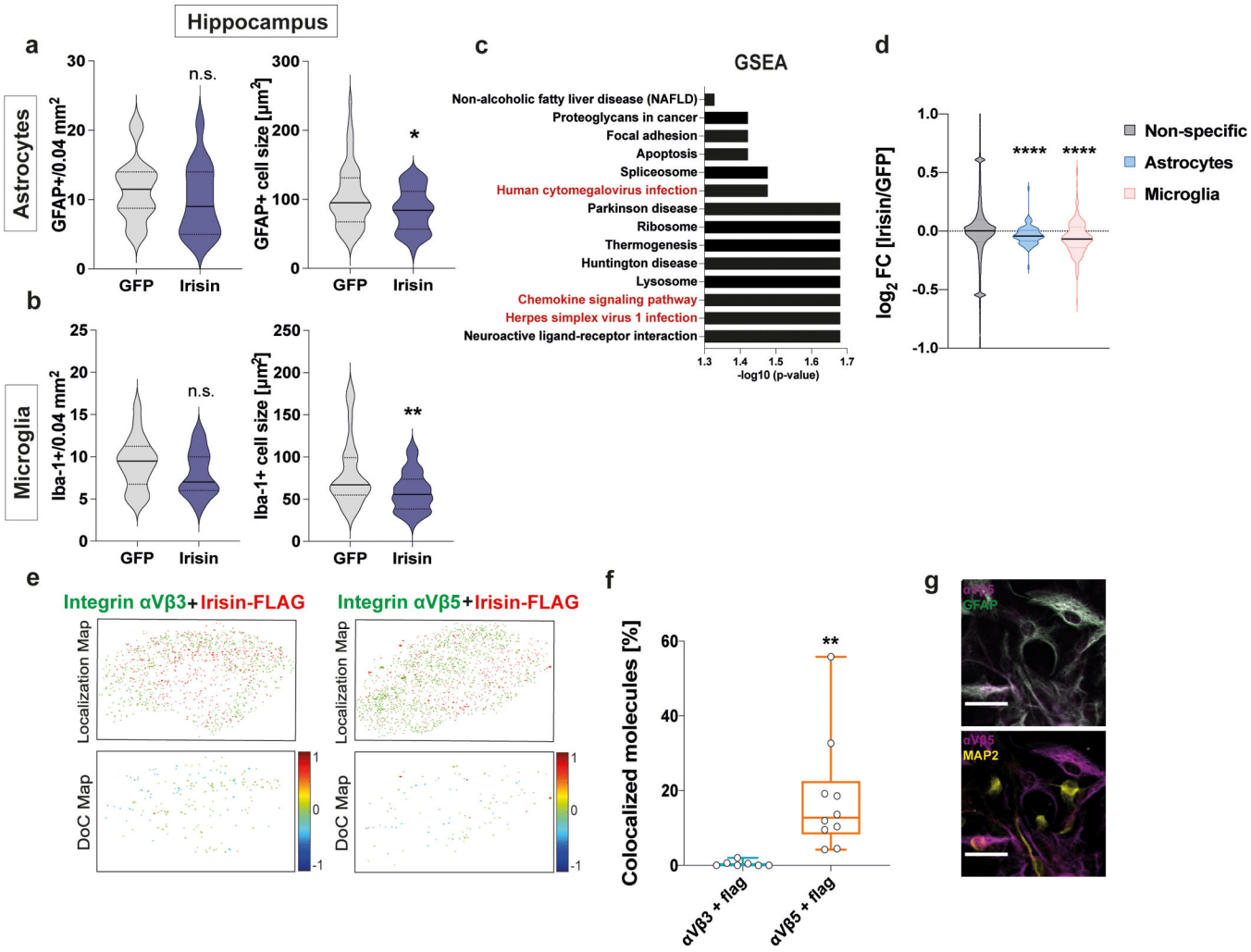

Fig. 7. Peripheral irisin reduces glia activation in transgenic mouse models of AD.

a-d, APP/PS1 mice were injected with AAV8-GFP or AAV8-irisin-FLAG via the tail vein. **a and b,** Quantification of number (left panel) and cell size (right panel) of GFAP+ astrocytes (**a**) (GFP n=18, irisin n=15) (left); (GFP n=52, irisin n=42 (right) and Iba1+ microglia (**b**) (GFP n=18, irisin n=15) (left); (GFP n=52, irisin n=43) (right). **c and d,** Bulk RNA-seq analysis of hippocampal samples, GSEA analysis for regulated pathways (red for inflammatory pathways) (**c**) and overrepresentation analysis of glia genes (**d**) (GFP n = 5, irisin n = 5). **e, f,** Two-color STORM experiment on differentiated adult hippocampal primary neuronal stem cell cultures incubated with recombinant irisin-FLAG. Clus-DoC localization map (top) for irisin-FLAG (red) and integrin αV/β3(left) or integrin αV/β5 (right) (both in green) and Clus-Doc Degree of colocalization (DoC) (bottom) for irisin-FLAG relative to integrin αV/β3 (left) or integrin αV/β5 (right). Co-localizations are color coded according to their DoC scores (score bar at the right of the bottom panels) **(e)** and quantification of colocalized molecules (Irisin-FLAG-αV/β3 n = 7, irisin-FLAG-αV/β5 n = 10) (**f**). **g,** Representative confocal images of co-localization of αV/β5 integrins (magenta) with GFAP+ astrocytes (green) (top) and MAP2+ neurons (yellow) (bottom). N = 3 per group. Scale bar 20 µm. Two-tailed t-test (**a**, **b**), two-tailed t-test with Welch's correction (**d,**

f). *p<0.05, **p<0.01, ****p<0.0001; n.s.= not significant. Data are represented as mean ± SEM of biologically independent samples, except for violin plots with center line = median, dotted line = upper and lower quartile (**d**) and box plots: center line = median, bound of box = 25^{th} to 75^{th} percentiles, whiskers = max to min (**f**). See source data for exact p-values.

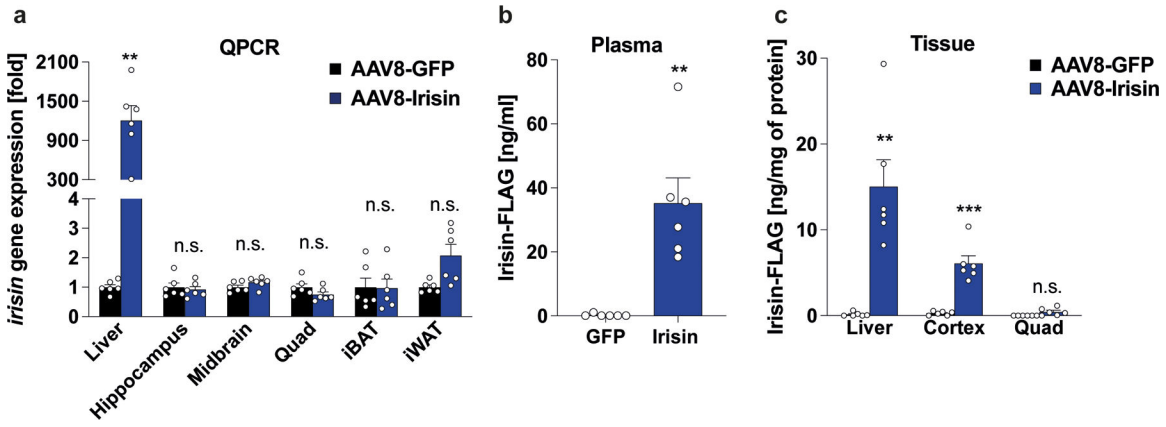

Fig. 8. Peripherally delivered irisin crosses the blood brain barrier.

WT mice were injected with AAV8-GFP or AAV8-irisin-FLAG via the tail vein. Tissues were collected three weeks later. **a,** qPCR analysis. **b,** Irisin-FLAG levels in plasma and **c,** tissue lysates by ELISA (n = 6 per group). Multiple t-tests with Bonferroni-Dunn method correction for adjusted p-value (**a, c**), Two-tailed t-test (**b**). **p<0.01, ****p <0.0001, n.s.= not significant. Data are represented as mean ± SEM of biologically independent samples. See source data for exact p-values.